

Ocean air masses dominate the land-surface atmospheric water cycles in the coastal areas of Liaodong Bay: Insights from stable isotopes

Yiyuan Du¹, Ri Hong Wen², Shristee Panthee³, Sissou Zakari⁴, Liang Song⁵, Wen-Jie Liu⁶, and Bin Yang³

¹University of Chinese Academy of Sciences

²China Meteorological Administration

³Xishuangbanna Tropical Botanical Garden, Chinese Academy of Sciences

⁴Univ Parakou

⁵Chinese Academy of Sciences (CAS)

⁶Xishuangbanna tropical botanical garden, Chinese academy of sciences

December 14, 2022

Abstract

Long-term atmospheric water vapor hydrogen ($\delta^2\text{H}$), oxygen ($\delta^{18}\text{O}$), and deuterium excess (d-excess) can provide unique insights into the land-atmosphere coupling processes. The in-situ measurements of atmospheric water vapor $\delta^2\text{H}$, $\delta^{18}\text{O}$, and d-excess were conducted above a reed wetland of Liaodong Bay (2019-2020). We found significant inter-annual variations in atmospheric water vapor isotopes between the two growing (May-September) seasons. The $\delta^2\text{H}$, $\delta^{18}\text{O}$, and d-excess of atmospheric water vapor exhibited different seasonal and diurnal cycles respect to the vertical (i.e., 1 m, 3 m, and 5 m) measurement heights, especially in 2019. The isotopic differences of atmospheric water vapor among vertical measurement heights were more evident in the daytime (8:00-20:00 LST) than at night (20:00-8:00 LST). Rainfall events had a direct impact on the diurnal patterns of water vapor isotopes, and the influences depended on rainfall intensities. However, only week correlations existed between water vapor isotopes and local meteorological factors ($R^2 = 0.01-0.16$, $P < 0.001$), such as water vapor concentration (w), relative humidity (RH), and surface air temperature (T_a). Based on the back-air trajectory analyses, the spatial-temporal dynamics of atmospheric water vapor isotopes highly synchronized with monsoon activities. The dominant air masses in this region mainly arose from ocean sources, which contributed to $62.1 \pm 12.2\%$ (49.4-84.5%) of the total air moisture. High d-excess consistently followed the strong monsoon activities, suggesting predominating impacts of ocean air masses from the East Asian monsoon region. High-resolution measurements of atmospheric water vapor isotopes will improve our understanding of the hydrological cycles in coastal areas.

Hosted file

951725_0_supp_10518903_rmkszz.doc available at <https://authorea.com/users/566185/articles/612953-ocean-air-masses-dominate-the-land-surface-atmospheric-water-cycles-in-the-coastal-areas-of-liaodong-bay-insights-from-stable-isotopes>

1 **Ocean air masses dominate the land-surface atmospheric water cycles in**
2 **the coastal areas of Liaodong Bay: Insights from stable isotopes**

3
4 **Yi-Yuan Du^{1,2*}, Ri-Hong Wen^{3*}, Shristee Panthee¹, Sissou Zakari⁶, Liang Song¹,**
5 **Wen-Jie Liu¹, Bin Yang^{1†}**

6 ¹CAS Key laboratory of Tropical Forest Ecology, Xishuangbanna Tropical Botanical
7 Garden, Chinese Academy of Sciences, Menglun 666303, Yunnan, China.

8 ²University of Chinese Academy of Sciences, Beijing 100049, China.

9 ³Institute of Atmospheric Environment, China Meteorological Administration,
10 Shenyang, 110166, Liaoning, China.

11 ⁴Laboratory of Hydraulics and Environmental Modeling, Faculty of Agronomy,
12 Université de Parakou, Parakou, 03 BP 351, Benin.

13

14 Corresponding author: Yang Bin (yangbin@xtbg.ac.cn)

15 Menglun Yunnan, China; Tel.: 19969108917; Fax: 86-691-8715070

16 **Key Points:**

- 17 • Spatial-temporal variations of water vapor isotopes are very different during
18 2019/2020 growing (May-September) seasons.
- 19 • Meteorological variables are not reliable indicators for water vapor $\delta^2\text{H}$, $\delta^{18}\text{O}$,
20 and d-excess at Panjin experimental station.
- 21 • Ocean air masses from East Asian monsoon dominate land-surface
22 atmospheric water vapor cycles in the coastal areas of Liaodong Bay.

23

24 **Abstract**

25 Long-term atmospheric water vapor hydrogen ($\delta^2\text{H}$), oxygen ($\delta^{18}\text{O}$), and deuterium
26 excess (*d-excess*) can provide unique insights into the land-atmosphere coupling
27 processes. The in-situ measurements of atmospheric water vapor $\delta^2\text{H}$, $\delta^{18}\text{O}$, and *d-*
28 *excess* were conducted above a reed wetland of Liaodong Bay (2019-2020). We found
29 significant inter-annual variations in atmospheric water vapor isotopes between the
30 two growing (May-September) seasons. The $\delta^2\text{H}$, $\delta^{18}\text{O}$, and *d-excess* of atmospheric
31 water vapor exhibited different seasonal and diurnal cycles respect to the vertical (i.e.,
32 1 m, 3 m, and 5 m) measurement heights, especially in 2019. The isotopic differences
33 of atmospheric water vapor among vertical measurement heights were more evident
34 in the daytime (8:00-20:00 LST) than at night (20:00-8:00 LST). Rainfall events had a
35 direct impact on the diurnal patterns of water vapor isotopes, and the influences
36 depended on rainfall intensities. However, only weak correlations existed between
37 water vapor isotopes and local meteorological factors ($R^2 = 0.01-0.16$, $P < 0.001$),
38 such as water vapor concentration (w), relative humidity (RH), and surface air
39 temperature (T_a). Based on the back-air trajectory analyses, the spatial-temporal
40 dynamics of atmospheric water vapor isotopes highly synchronized with monsoon
41 activities. The dominant air masses in this region mainly arose from ocean sources,
42 which contributed to $62.1 \pm 12.2\%$ (49.4-84.5%) of the total air moisture. High *d-*
43 *excess* consistently followed the strong monsoon activities, suggesting predominating
44 impacts of ocean air masses from the East Asian monsoon region. High-resolution
45 measurements of atmospheric water vapor isotopes will improve our understanding of
46 the hydrological cycles in coastal areas.

47 **Plain Language Summary**

48 The coastal wetland regions in East Asia always have complex atmospheric
49 hydrological processes, because they are influenced both by the westerly belt and the
50 East Asian monsoon. Under such circumstances, still the question remains how do the
51 multiple air masses affect the seasonal and diurnal patterns of atmospheric
52 circulations? We implemented high temporal resolution (1Hz) measurements of
53 atmospheric hydrogen ($\text{HDO}/\text{H}_1\text{H}_2^{18}\text{O}$) and oxygen (H_2^{18}O and H_2^{16}O) using an off-
54 axis integrated cavity output spectroscopy (OA-ICOS) technology in a reed wetland.
55 The deuterium excess ($d\text{-excess} = \delta^2\text{H} - 8 \times \delta^{18}\text{O}$) of atmospheric water vapor was
56 further used as an indicator for identifying the moisture source locations (2019-2020).
57 There were obvious seasonal and diurnal variations of atmospheric water vapor $\delta^2\text{H}$,
58 $\delta^{18}\text{O}$, and *d-excess*. However, the inter-annual variations in atmospheric water vapor
59 isotopes were more notable in this study, mainly due to the stronger monsoon
60 activities. For example, the landing of typhoon “Lekima” brought a very high level of
61 atmospheric water vapor *d-excess* in 2019. Therefore, the local meteorological
62 variables might not be sufficient predictors of the atmospheric water vapor isotopes in
63 the coastal wetland regions.

64 **1 Introduction**

65 Measurements of atmospheric water vapor hydrogen ($\delta^2\text{H}$), oxygen ($\delta^{18}\text{O}$),
66 and deuterium excess (*d-excess*) can provide unique insights into the land-atmosphere
67 coupling processes (Gat, 1996; Lee et al., 2005; Vuille et al., 2003). The $\delta^2\text{H}$, $\delta^{18}\text{O}$,
68 and *d-excess* of water vapor (termed as the δ_{vapor} hereafter) can be used as natural
69 tracers of atmospheric water cycles (Bastrikov et al., 2014; Christner et al., 2017;
70 Munksgaard et al., 2020; Wen et al., 2008, 2010). Influenced by lower tropospheric
71 water variations (e.g., precipitation and vertical atmospheric mixing) and local
72 vegetation properties (e.g., soil evaporation and plant transpiration), the signatures of
73 land-surface water vapor δ_{vapor} contain subtle information concerning water
74 movements between the atmospheric boundary layer (ABL) and Earth's surfaces
75 (Huang & Wen, 2014; Laonamsai et al., 2021; Lee et al., 2006). Thus, there is a
76 growing interest in high-resolution measurements of atmospheric water vapor δ_{vapor}
77 from ecosystem to regional scales (Galewsky et al., 2016; Steen-Larsen et al., 2013;
78 Wei & Lee, 2019). Several studies have successfully completed the in-situ
79 atmospheric water vapor δ_{vapor} monitoring based on the technological advantages of
80 laser spectrometers (Aemisegger et al., 2014; Hu et al., 2014; Noone et al., 2012).
81 However, it is still necessary to conduct in-situ measurements of atmospheric water
82 vapor δ_{vapor} above near-surface ecosystems (Galewsky et al., 2016; Lee et al., 2005,
83 2007), compared with the condensed water isotopes that have formed a well-known
84 global network (e.g., Global Network of Isotopes in Precipitation, GNIP).

85 To the best of our knowledge, datasets of in-situ atmospheric water vapor
86 δ_{vapor} are reported across 49 sites worldwide. Those sites reflect the global land
87 surface in all forms, including oceans (e.g., Bonne et al., 2019; Galewsky et al., 2022;
88 Steen-Larsen et al., 2014a), forests (Aron et al., 2019; Bastrikov et al., 2014; Mercer
89 et al., 2020), grasslands (Hu et al., 2014; Parkes et al., 2017; Tremoy et al., 2014),
90 croplands (Griffis et al., 2016; Huang & Wen, 2014; Wen et al., 2012), ice sheets
91 (Bonne et al., 2020; Casado et al., 2016; Steen-Larsen et al., 2014b), cities (Christner
92 et al., 2017; Noone et al., 2012; Wang et al., 2021), and lakes (Cui et al., 2018; Hu et
93 al., 2021; Xiao et al., 2017). These studies confirm the great potential of in-situ water
94 vapor δ_{vapor} measurements to deconstruct the complex hydrological processes.
95 However, among the available data on atmospheric water vapor δ_{vapor} , the data from
96 coastal wetlands are scarce (Delattre et al., 2015; Lai et al., 2018). For example,
97 Delattre et al. (2015) showed that ground level atmospheric vapour composition can
98 record both local and regional isotopic signatures during 36 consecutive summer
99 days. The water vapor δ_{vapor} data reported by Lai et al. (2018) showed that, on daily
100 time scales (11-28 July, 2017), substantial rain recycling and large-scale atmospheric
101 water transport occur above a coastal mangrove forest in southern China, which is
102 subjected to the monsoons from South China Sea, Indian Ocean, Pacific Ocean, and
103 local land areas. Nevertheless, the brief campaigns of water vapor δ_{vapor} measurements
104 would restrain the best demonstration of atmospheric processes in the coastal
105 wetlands.

106 Previous studies have demonstrated that the small spatial and temporal variations of
107 atmospheric water vapor δ_{vapor} are affected mainly by processes of atmospheric
108 entrainments, land surface evapotranspiration (i.e., soil evaporation and plant
109 transpiration, ET), and vapor condensations (Huang & Wen, 2014; Lee et al., 2007;
110 Fiorella et al., 2019; Diekmann et al., 2021). Entrainment processes of the free
111 atmosphere will vertically deplete the ^2H and ^{18}O of water vapor near the land
112 surfaces (Devi et al., 2014; Kurita et al., 2012; Wei et al., 2015). Local ET will enrich
113 the ^2H and ^{18}O of near-surface atmosphere above the densely vegetated landscapes,
114 which usually plays a dominant role in the variations of water vapor δ_{vapor} (Lai &
115 Ehleringer, 2011; Zhang et al., 2011). The diurnal dynamics of atmospheric water
116 vapor δ_{vapor} are closely associated with the vapor condensation processes (e.g.,
117 precipitation, dew and fog), which is mainly caused by the equilibrium phase changes
118 of local water vapor during the synoptic events (Bailey et al., 2015; Farlin et al., 2013;
119 Wen et al., 2012). On large spatial scales, air mass advection is considered as a
120 critical factor contributing to the temporal variability in atmospheric water vapor δ_{vapor}
121 (Dahinden et al., 2021; Galewsky et al., 2011; Steen-Larsen et al., 2015).

122 Despite high-resolution monitoring efforts over the past two decades,
123 decoupling the atmospheric water vapor δ_{vapor} variability across various timescales
124 remains challenging (Bagheri et al., 2019; Berkelhammer et al., 2013; Lee et al.,
125 2005; Dahinden et al., 2021). The deuterium excess ($d\text{-excess} = \delta^2\text{H} - 8 \times \delta^{18}\text{O}$) of
126 atmospheric water vapor provides a new insight into the source identification of
127 atmospheric moistures (Dansgaard, 1964; Merlivat & Jouzel, 1979; Welp et al.,
128 2012). The theoretical basis of this application is that the $d\text{-excess}$ of water vapor is
129 closely linked to the environmental conditions during the kinetic fractionation
130 processes (Araguas-Araguas et al., 2000; Craig, 1961). Hence, the strong sensitivity
131 of $d\text{-excess}$ to local atmosphere relative humidity (RH) can place better constraints on
132 the water transport processes than the analyses of water vapor $\delta^2\text{H}$ and $\delta^{18}\text{O}$ alone
133 (Lai et al., 2018; Wei & Lee, 2019). Previous work has traced both the ocean moisture
134 sources (Dahinden et al., 2021; Gonzalez et al., 2016; Salamalikis et al., 2015) and
135 continental moisture recycling (Aemisegger et al., 2014; Fiorella et al., 2019). To
136 better resemble the transmission path of large-scale air masses, tools of Hybrid
137 Single-Particle Lagrangian Integrated Trajectory (HYSPPLIT) and TrajStat models
138 have been widely used in conjunction with water vapor isotopes in recent years
139 (Bagheri et al., 2019; Fiorella et al., 2018; Gonzalez et al., 2016; Salamalikis et al.,
140 2015). It is foreseeable that long-term water vapor $d\text{-excess}$ measurements will
141 improve our understanding of atmospheric processes and the associated mechanisms
142 in the coastal wetlands.

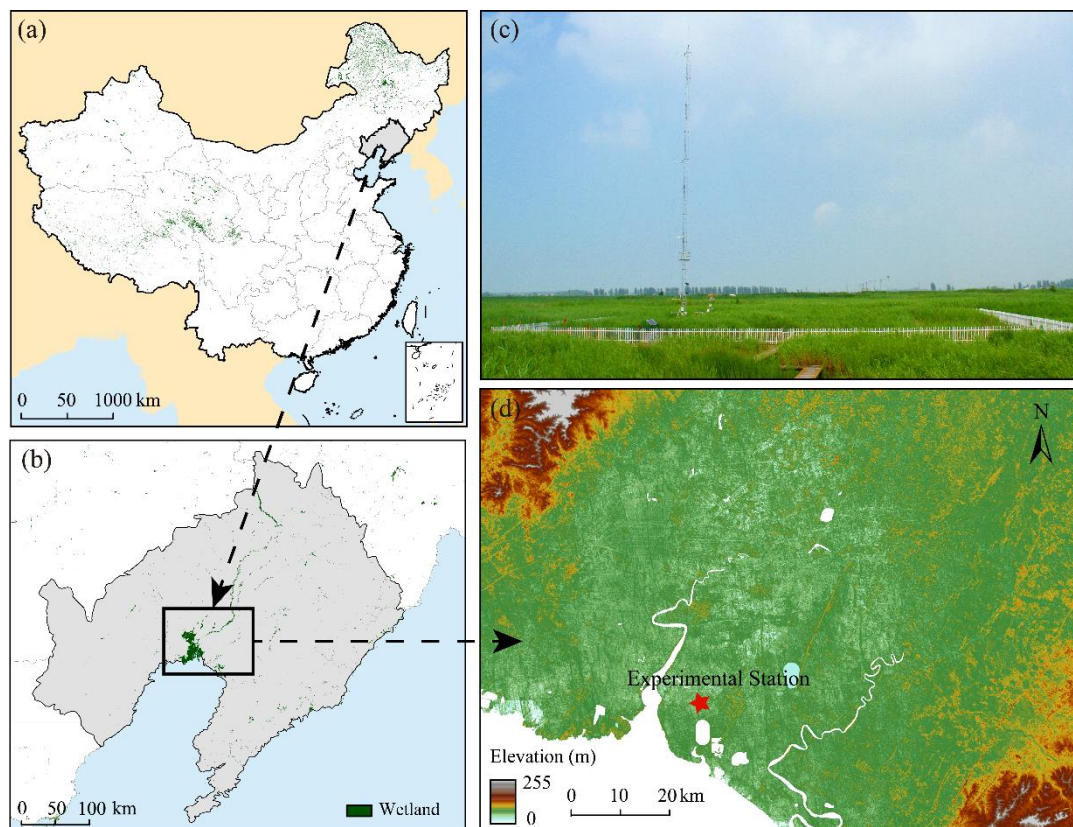
143 Liaodong Bay, a high-latitude continental bay (37.1-41.0° N, 117.6-121.2° E),
144 has the largest size and northernmost semi-enclosed seaports in China. It contains a
145 wetland area of approximately 5300 km² (Luo et al., 2021). According to the 2nd
146 National Wetland Survey Statistics Report (NFGA, 2010), the reed wetlands in this
147 region are well-preserved and among the largest in extent (~ 2500 km²) in the world.
148 Those offshore wetlands are located in the transition zones between continents and
149 oceans, which are vulnerable to natural and anthropogenic activities, such as urban

150 and agricultural runoff. To fill the gaps in knowledge regarding the mechanisms of
151 water cycle processes, we conducted two-year (2019-2020) measurements of
152 atmospheric water vapor $\delta^2\text{H}$, $\delta^{18}\text{O}$, and *d-excess* in the reed wetlands of Liaodong
153 Bay. The present study aims to (i) investigate the spatial-temporal dynamics of
154 atmospheric water vapor isotopes above the coastal wetland, and (ii) identify the
155 contributing factors that affect the isotopic characteristics of atmosphere in Liaodong
156 Bay. We hypothesize that (1) isotopic gradients exist for atmospheric water vapor
157 measurements along the monitoring heights due to the growth of reeds, and (2) moist
158 air masses from the East Asian monsoon strongly affects the atmospheric water vapor
159 isotopes.

160 **2 Materials and Methods**

161 2.1 Study site

162 The observations were carried out at Panjin Wetland Field Science
163 Experimental Station (40° 56' 40" N, 121° 56' 36" E, and elevation 2.1 m), located in
164 the north of Liaodong Bay. This station is a member of the National Climatic
165 Observatory of China Meteorological Administration (CMA), which is adjacent to the
166 Liaohe River Delta wetlands, and 12 km to the Bohai Sea (Figure 1a and 1b). This
167 area is characterized by the semi-humid temperate monsoon climate, influenced by
168 the westerly belt and the East Asian monsoon. The southwest East Asian monsoon
169 prevails from May to September, which brings abundant rainfall between July and
170 September (Huang et al., 2018). The regional meteorological records (1961-2010)
171 indicate that the mean air temperature and annual precipitation are 9.1 °C and 643.9
172 mm, respectively. Approximately 170 days of frost-free weather occur throughout the
173 year. The annual evaporation is about 516.0-720.3 mm (2012-2015). The research site
174 (150 m × 150 m) is situated in the center of a reed marsh (~ 780 km²), with a
175 vegetation coverage of more than 90% (Wang et al., 2016). Meteorological data of
176 surface air temperature (T_a), relative humidity (RH), and total precipitation (P)
177 obtained from an automatic weather station (Model A753WS, Adcon Telemetry Inc.,
178 Santa Rosa, CA). The leaf area index (LAI) and height of the reeds were collected for
179 fifteen days intervals during the growing season (May-September). During the study
180 periods of 2019 and 2020, the maximum LAI and maximum height were 5.1 m² m⁻²
181 and 2.5 m, respectively.



182

183 **Figure 1.** Maps showing the locations of Liaodong Bay (a, b) and Panjin
 184 experimental station (c, d) in this study. Elevation data was downloaded from the
 185 National Earth System Science Data Center, National Science & Technology
 186 Infrastructure of China (<http://www.geodata.cn>).

187

2.2 In-Situ measurement of water vapor isotopes

188

189

190

191

192

193

194

195

196

197

198

199

200

201

202

203

204

The in-situ system used to measure the atmospheric water vapor $\delta^2\text{H}$ and $\delta^{18}\text{O}$ consisted of a water vapor isotope analyzer (WVIA), a water vapor isotope standard source (WVISS), and an air sampling system (ASS). The WVIA was used to measure water vapor isotopes (at a frequency of 1 Hz) based on the off-axis integrated cavity output spectroscopy (OA-ICOS; Model TIWA-912, Los Gatos Research, Mountain View, CA, USA). The analyzer has a near-infrared diode laser scanning absorption lines ($\sim 1.4 \mu\text{b}$) for H_2^{16}O , H_2^{18}O , and $\text{H}_1\text{H}_2^{16}\text{O}$ (HDO), whose precision was approximately 0.4‰ for $\delta^2\text{H}$ and 0.08‰ for $\delta^{18}\text{O}$ (Steen-Larsen et al., 2013; Wen et al., 2012). The WVISS is an online calibration device that generates fixed concentrations of continuous vapor streams (Model 908-004-902, Los Gatos Research, Mountain View, CA, USA). In this study, ultrapure liquid water with known isotopic values was nebulized (at a rate of $2\text{-}10 \text{ L min}^{-1}$) to produce three designated gradients of standard streams (S_1 , S_2 , and S_3 , 300s each) covering the water vapor concentration of ambient air. There is no isotopic fractionation since the nebulizer and hot chamber (2 L) of WVISS will ensure instant evaporation (heated to $80 \text{ }^\circ\text{C}$) of all liquid water. The ASS was mounted on a 30 m height tower (Figure 1c) and used to pump ambient air from four heights (1, 3, 10, and 15 m) with 300s spent

205 on each height. To reduce the residence time of ambient air in the inlet lines (i.e.,
 206 “memory effects”), the sampling lines were pumped at approximately 2 L min⁻¹ using
 207 a commercial multiplexer (Model MC-2000-8, Lica United Technology Limited Inc.,
 208 Beijing, CHN). Teflon pipes were used in conjunction with individual heating tapes
 209 and jackets to prevent possible vapor condensation in the sampling tubes (Lee et al.,
 210 2005; Sturm & Knohl, 2010). Filters were installed at the entrances of the air-intake
 211 lines to prevent sucking liquid water into the instrument (Model 300-01961, LI-COR
 212 Inc., Lincoln, NE, USA). The switching sequence was S₁, S₂, S₃, and ambient air,
 213 with 15 minutes on the standard streams and 220 minutes on ambient air. The WVIA
 214 and WVISS were placed in an air-conditioning room to minimize the temperature-
 215 driven drifts.

216 While using the OA-ICOS for high-precision measurements of atmospheric
 217 water vapor $\delta^2\text{H}$ and $\delta^{18}\text{O}$, measurement bias can occur because of the instrumental
 218 concentration-dependence and time-drift (Bastrikov et al., 2014; Wen et al., 2008,
 219 2012). Here, we followed a user-configurable “two-point calibration” protocol
 220 described by Wen et al. (2012), Huang & Wen (2014) and Xiao et al. (2017). Every
 221 220 minutes (i.e., ~ 3.7 h) after the ambient (1, 3, 10, and 15 m) air measurements,
 222 two of the three standards (S₁, S₂, and S₃) spanning the water vapor concentration of
 223 ambient air were used to linearly calibrate atmospheric water vapor measurements.
 224 The isotopic values of the liquid calibration standards were measured using a liquid
 225 water isotope analyzer (Model GLA 431-TLWIA, Los Gatos Research, Mountain
 226 View, CA, USA), which were scaled to the Vienna Standard Mean Ocean Water
 227 (VSMOW) scale. For all the raw $\delta^2\text{H}$ and $\delta^{18}\text{O}$ measurements, the first 180 of 300 s
 228 spent measuring a given standard stream or an ambient vapor were discarded from the
 229 analysis to eliminate the possible memory effects. Then, the “two-point” linear
 230 interpolation was implemented using the following formula (Wen et al., 2012; Huang
 231 & Wen, 2014):

$$232 \quad \delta_{\text{vapor}} = \delta_{s1} + \frac{(\delta_{s2} - \delta_{s1})}{(X_{s2} - X_{s1})} \times (X_{\text{air}} - X_{s1}) \quad (1)$$

233 where δ_{vapor} is the isotopic ratio ($^2\text{H}/^1\text{H}$, or $^{18}\text{O}/^{16}\text{O}$) of one ambient air (i.e., 1,
 234 3, 10, and 15 m), δ_{s1} and δ_{s2} are the single-point corrected ambient airs that are
 235 normalized to a reference humidity (i.e., X_{s1} and X_{s2}), X_{s1} , X_{s2} and X_{s1} are water
 236 vapor concentrations of the two selected standard streams (S₁, S₂, and S₃) and the
 237 ambient air, respectively.

238 The isotopic data collected at 1 m, 3 m, and 15 m in height were used for
 239 representing the lower, middle, and upper canopy during the 2019-2020 growing
 240 (May-September) seasons. The second-order parameter deuterium excess ($d\text{-excess} =$
 241 $\delta^2\text{H} - 8 \times \delta^{18}\text{O}$) is defined as the deviation from the linear relationship between $^2\text{H}/^1\text{H}$
 242 and $^{18}\text{O}/^{16}\text{O}$ in the Global Meteoric Water Line (GMWL) having a mean slope of 8
 243 (Dansgaard, 1964; Merlivat & Jouzel, 1979). All data reported were block-averaged
 244 to hourly intervals.

245 2.3 Back-air mass trajectory analyses

246 The Hybrid Single Particle Lagrangian Integrated Trajectory (HYSPLIT)
 247 model was used to track changes in isotopic composition and moisture sources
 248 (Christner et al., 2018; Munksgaard et al., 2020). The HYSPLIT model
 249 (<https://ready.arl.noaa.gov/HYSPLIT.php>) was developed by the National Oceanic
 250 and Atmospheric Administration-Air Resources Laboratory (NOAA-ARL). Inputs of
 251 the HYSPLIT model include the cloud height, wind direction, temperature, and
 252 surface pressure, which are available from the Global Data Assimilation System
 253 (GDAS) meteorological data. In this study, the spatial resolution of the HYSPLIT
 254 model was set to $1^\circ \times 1^\circ$, and the starting height was set to 500 m above ground level.
 255 The 48-hour back-tracking analysis (close to the time that water vapor is present in
 256 the air) was performed hourly for the experimental site from May to September 2019
 257 and 2020. The angular distance of the TrajStat model
 258 (<http://www.meteothinker.com/downloads/index.html>) was used to cluster the
 259 trajectories of air mass reaching the experimental station:

$$260 \quad D = \frac{1}{n} \sum_{i=1}^n \left(0.5 \frac{A_i + B_i - C_i}{\sqrt{A_i B_i}} \right) \quad (2)$$

261 where D is the average angular distance between two backward trajectories, A
 262 and B are the squares of the straight-line distances between the trajectory points and
 263 the experimental site, and C denotes the square of the straight-line distance between
 264 the two trajectory points.

265 The Concentration Weighted Trajectory (CWT) method was used to identify
 266 the potential source regions contributing to the variability of atmospheric water vapor
 267 *d-excess* at the experimental site (Li et al., 2020; Salamalikis et al., 2015). The
 268 rearward trajectories were assigned by the equally sized $i \times j$ grid cells. The sample
 269 concentrations accompanying trajectories that traversed each grid cell were averaged
 270 to provide each grid cell with a weighted concentration. The calculation of this
 271 method could be found in Li et al. (2020):

$$272 \quad C_{ij} = \frac{1}{\sum_{l=1}^M \tau_{ijl}} \sum_{l=1}^M c_l \tau_{ijl} \quad (3)$$

273 where C_{ij} is the average *d-excess* concentration in the ij^{th} cell, l is the
 274 trajectory index, M is the total number of the trajectories, c_l is the concentration (*d-*
 275 *excess*) of the trajectory l , and τ_{ijl} is the time spent in the ij^{th} cell by the trajectory l .
 276 The weight function (W_{ij}) was further introduced ($WCWT_{ij} = C_{ij} \times W_{ij}$) to reduce
 277 uncertainty because the error of CWT increases with the distance between the grid
 278 and the experimental station.

279 2.4 Statistical analyses

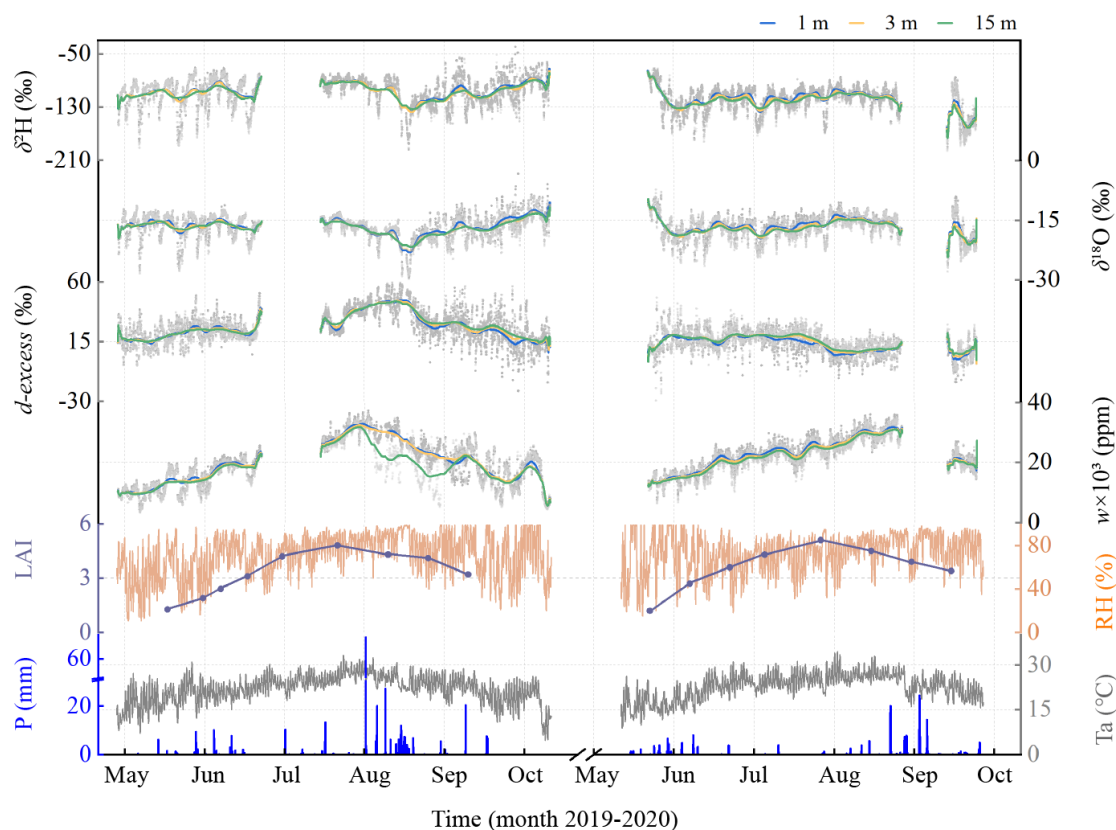
280 The isotopic data of atmospheric water vapor were calibrated based on the
281 “two-point calibration” protocol using Matrix Laboratory (MATLAB, version 9.2.0,
282 The MathWorks, Inc. Natick, USA). The normality and homogeneity of all data were
283 checked using IBM SPSS statistical software (Version 22.0, SPSS Inc., Chicago,
284 USA). One-way analysis of variance (ANOVA) and multiple means comparisons
285 (LSD) were used to highlight differences in data between months and vertical strata.
286 Considering the possible errors of the two variables, we used geometric mean
287 regression (GMR) to assess the relationships between atmospheric water vapor
288 isotopes and meteorological data with two probability levels of $P \leq 0.05$ and $P \leq$
289 0.001 .

290 **3 Results**

291 3.1 Long time scale variations

292 Figure 2 shows the seasonal variations in hourly measured atmospheric water
293 vapor $\delta^2\text{H}$, $\delta^{18}\text{O}$, and *d-excess* at lower (1 m), middle (3 m), and upper (15 m)
294 measurement heights during the 2019-2020 growing (May-September) seasons. The
295 meteorological data of water vapor concentration (*w*), leaf area index (LAI), relative
296 humidity (RH), total precipitation (P), and surface air temperature (T_a) are also
297 presented for the Panjin experimental station. The WVIA analyzer was under repairs
298 from June 20 to July 10, 2019, and from August 24 to September 9, 2020. For the rest
299 of the study periods, only short gaps occurred in the in-situ measurements of
300 atmospheric water vapor $\delta^2\text{H}$, $\delta^{18}\text{O}$, and *d-excess* due to the occasional system
301 downtimes (e.g., electricity interruption and/or analyzer breakdown). The monthly
302 average of the above isotopic values of atmospheric water vapor and meteorological
303 data are summarized in Table 1.

304 The $\delta^2\text{H}$, $\delta^{18}\text{O}$, and *d-excess* of atmospheric water vapor underwent
305 pronounced inter-annual and annual changes with months and vertical measurement
306 heights (Figure 2). Significant differences existed in atmospheric water vapor $\delta^2\text{H}$ (P
307 < 0.001), $\delta^{18}\text{O}$ ($P < 0.05$), and *d-excess* ($P < 0.001$) between 2019 and 2020. The
308 mean isotopic values of atmospheric water vapor were higher in 2019 ($\delta^2\text{H}$: $-108.4 \pm$
309 21.4‰ , $\delta^{18}\text{O}$: $-16.64 \pm 3.13\text{‰}$, and *d-excess*: $26.3 \pm 11.7\text{‰}$) than in 2020 ($-120.7 \pm$
310 20.2‰ , $-16.98 \pm 2.93\text{‰}$ and $13.3 \pm 8.4\text{‰}$). Variation amplitudes (i.e., maximums –
311 minimums) of the water vapor $\delta^2\text{H}$, $\delta^{18}\text{O}$, and *d-excess* were 153.8‰, 27.69‰, and
312 82.5‰ in 2019, and were 124.5‰, 20.78‰, and 77.7‰ in 2020. The $\delta^2\text{H}$ and $\delta^{18}\text{O}$ of
313 atmospheric water vapor gradually decreased with the vertical measurement heights
314 from 1 m to 3 m and 15 m in both 2019 and 2020. In contrast, the *d-excess* of water
315 vapor increased from the lower (1 m) to the upper (15 m) canopy during the two years
316 of study periods. The difference in atmospheric water vapor $\delta^2\text{H}$, $\delta^{18}\text{O}$, and *d-excess*
317 was only significant between 1 m and 15 m ($P < 0.05$) in 2019. The isotopic values of
318 atmospheric water vapor changed drastically between 1 m and 15 m ($P < 0.001$) in
319 2020; and the atmospheric water vapor $\delta^{18}\text{O}$ and *d-excess* differed significantly
320 between 1 m and 3 m ($P < 0.001$) in 2020.



321

322 **Figure 2.** Time series of hourly atmospheric water vapor $\delta^2\text{H}$, $\delta^{18}\text{O}$, and $d\text{-excess}$,
 323 water vapor concentration (w), leaf area index (LAI), relative humidity (RH),
 324 precipitation (P), and surface air temperature (T_a) during the 2019-2020 growing
 325 (May-September) seasons. The Gaussian smoothing curves are shown for the in-situ
 326 atmospheric water vapor measurements at heights of 1 m (blue lines), 3 m (yellow
 327 lines), and 15 m (green lines).

328 The w of atmospheric water vapor was highest in August with single-peaked
 329 curves of seasonal variations (Figure 2). However, the peak of water vapor w in 2019
 330 (36959.8 ppm) was delayed for 25 days compared to the peak (36090.8 ppm) in 2020.
 331 Furthermore, there were apparent differences in the atmospheric water vapor w
 332 between 1 m (or 3 m) and 15 m in 2019 ($P < 0.001$). During the growing (May-
 333 September) seasons, the LAI of reeds were 3.3 ± 1.2 in 2019 and 3.6 ± 1.2 in 2020.
 334 The mean RH in 2019 and 2020 were 70.7 ± 19.7 and 72.6 ± 17.5 , respectively. The
 335 total rainfall was 37.6% lower in 2020 (414.1 mm) compared to 2019 (663.8 mm),
 336 indicating a weak summer monsoon year in 2020. The T_a of the experimental station
 337 was relatively constant with mean values of 21.9 ± 4.7 °C in 2019 and 22.8 ± 4.3 °C
 338 in 2020 during the study periods.

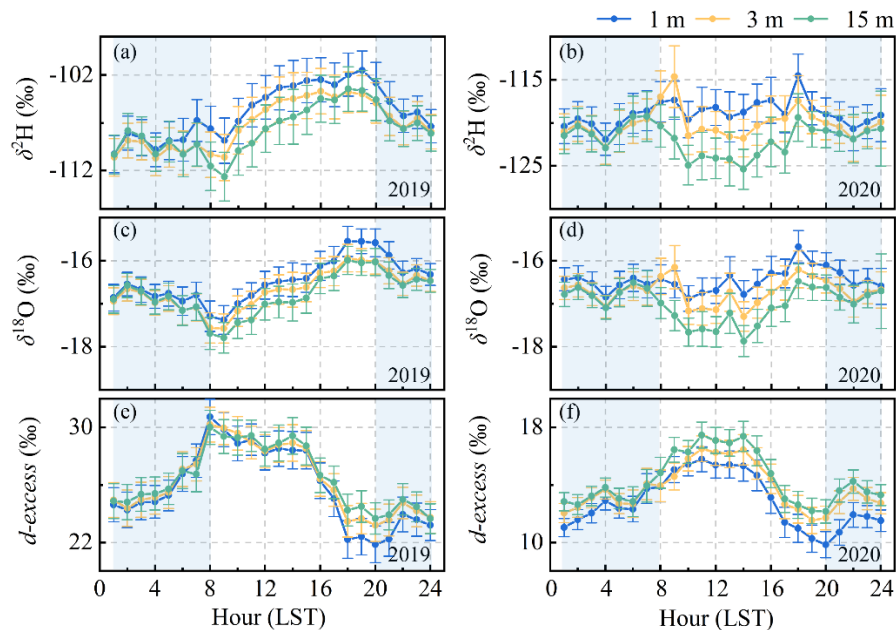
339 **Table 1** Monthly average values of Water Vapor Concentration (w), Leaf Area Index (LAI), Relative Humidity (RH), Total
 340 Precipitation (P), Surface Air Temperature (T_a), and Isotopic Values of Atmospheric Water Vapor ($\delta^2\text{H}$, $\delta^{18}\text{O}$, and $d\text{-excess}$) in
 341 Liaodong Bay, China, from May-September 2019 and 2020

Month	w (ppm) ^a	LAI (m ² m ⁻²)	RH (%)	P (mm)	T_a (°C)	$\delta^2\text{H}$ (‰)			$\delta^{18}\text{O}$ (‰)			$d\text{-excess}$ (‰)		
						1 m	3 m	15 m	1 m	3 m	15 m	1 m	3 m	15 m
May	12045.5	1.6	54.1	66.1	18.3	-111.1	-111.8	-112.5	-16.31	-16.40	-16.49	19.4	19.4	19.4
Jun	18875.6	3.3	69.4	44.9	22.0	-104.4	-105.8	-107.2	-16.10	-16.25	-16.31	24.4	24.2	23.3
Jul	29870.6	4.4	78.	55.8	25.6	-97.2	-97.5	-98.3	-12.79	-12.88	-13.00	33.7	34.1	34.2
Aug	25471.5	4.0	82.6	424.1	24.9	-113.2	-114.3	-115.0	-18.54	-18.77	-18.87	35.2	35.8	35.9
Sep	18040.9	3.2	70.1	107.9	26.0	-102.6	-104.9	-104.5	-15.47	-15.91	-16.02	21.2	22.2	23.4
May	14714.6	1.8	70.2	85.9	16.7	-117.9	-118.8	-119.2	-16.75	-16.93	-16.96	15.9	16.4	16.3
Jun	20746.6	3.4	64.6	29.2	23.1	-118.3	-120.3	-122.4	-16.99	-17.34	-17.61	17.6	18.4	18.6
Jul	25200.8	4.5	70.7	11.5	25.4	-113.1	-114.8	-116.3	-15.60	-16.03	-16.34	11.7	13.3	14.6
Aug	30488.3	4.2	80.6	253	25.5	-115.0	-115.7	-116.7	-15.46	-15.60	-15.76	8.6	9.0	9.4
Sep	20180.2	3.3	77.6	34.8	21.7	-144.3	-146.1	-148.7	-18.73	-19.09	-19.54	5.6	6.6	7.6

342 ^a The monthly w of atmospheric water vapor was calculated based on the average of data from the lower (1 m), middle (3 m), and
 343 upper (15 m) canopy.
 344

345 3.2 Long time scale variations

346 Figure 3 presents the diurnal variations of atmospheric water vapor $\delta^2\text{H}$, $\delta^{18}\text{O}$, and d -
 347 *excess* measured at heights of 1 m, 3 m, and 15 m. A clear diurnal cycle of water vapor $\delta^2\text{H}$,
 348 $\delta^{18}\text{O}$, and d -*excess* existed in both 2019 and 2020. The atmospheric water vapor $\delta^2\text{H}$ and $\delta^{18}\text{O}$
 349 generally increased from 9:00 (LST) to 18:00 (LST). Simultaneously, the $\delta^2\text{H}$ and $\delta^{18}\text{O}$ of water
 350 vapor progressively declined to their minimum around 8:00-9:00 (LST) on the next day (Figure
 351 3a-d). The diurnal variations of atmospheric water vapor $\delta^2\text{H}$ and $\delta^{18}\text{O}$ were less pronounced in
 352 2020 than in 2019. Nonetheless, the diurnal variations of atmospheric water vapor d -*excess* were
 353 pretty clear in both years of 2019 and 2020, which had an opposite diurnal trend to that of
 354 atmospheric water vapor $\delta^2\text{H}$ and $\delta^{18}\text{O}$ (Figure 3e-f). The isotopic differences of atmospheric
 355 water vapor across measurement heights (i.e., 1, 3, and 15 m) were more evident in the daytime
 356 (8:00-20:00 LST) than at night (20:00-8:00 LST). This phenomenon appeared extremely typical
 357 in 2020, during which the atmosphere water vapor $\delta^2\text{H}$ and $\delta^{18}\text{O}$ declined progressively with the
 358 increase of heights ($P < 0.05$).

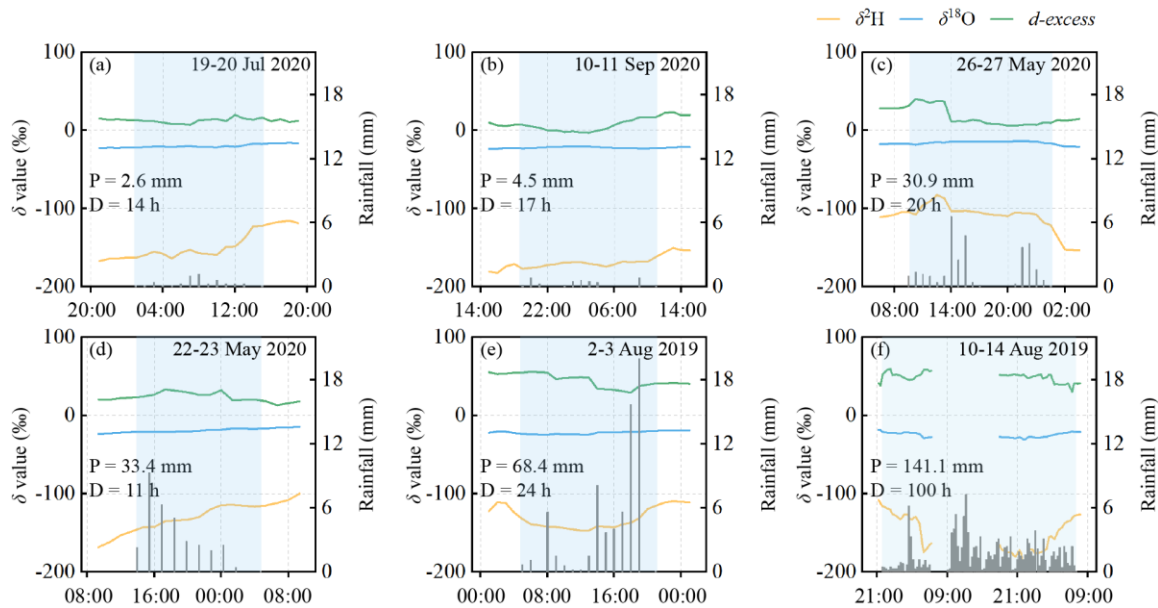


359

360 **Figure 3.** Twenty-four-hour variations of atmospheric water vapor $\delta^2\text{H}$ (a, b), $\delta^{18}\text{O}$ (c, d), and d -
 361 *excess* (e, f) measured at heights of 1 m (blue lines), 3 m (yellow lines), and 15 m (green lines)
 362 during the 2019-2020 growing (May-September) seasons. Error bars represent standard errors of
 363 the isotopic data in every hour. Shadow areas indicate the periods of time at night (20:00-8:00
 364 LST).

365 Figure 4 illustrates the impacts of rainfall processes on the diurnal cycles of atmospheric
 366 water vapor $\delta^2\text{H}$, $\delta^{18}\text{O}$, and d -*excess* at 15 m height. Six rainfall events of different rainfall
 367 amounts ($P = 2.6$ - 141.1 mm) were selected during the 2019-2020 growing (May-September)
 368 seasons. The duration (D) of these rainfall events ranged from 11 h to 100 h. The $\delta^2\text{H}$, $\delta^{18}\text{O}$, and
 369 d -*excess* of atmospheric water vapor increased slightly after two small rainfall events ($P = 2.6$ -
 370 4.5 mm, in Figure 4a-b). The peak-to-peak variations of atmospheric water vapor $\delta^2\text{H}$, $\delta^{18}\text{O}$, and
 371 d -*excess* were 31.8-51.6‰, 3.08-7.02‰, and 12.7-26.2‰, respectively. With the increase in

372 intensity and duration of rainfall, the isotopic values of atmospheric water vapor also increased
 373 during the rainfall processes (Figure 4c-d). However, the isotopic values of atmospheric water
 374 vapor declined after a 20 h continuous rainfall event. The variability of atmospheric water vapor
 375 in these moderate rainfall events ($P = 30.9\text{-}33.4$ mm) increased to $68.4\text{-}70.8\text{‰}$ for $\delta^2\text{H}$, 7.15-
 376 8.87‰ for $\delta^{18}\text{O}$, and $20.3\text{-}34.3\text{‰}$ for $d\text{-}excess$. The $\delta^2\text{H}$, $\delta^{18}\text{O}$, and $d\text{-}excess$ of atmospheric water
 377 vapor decreased drastically during the heavy rainfall events as expected (Figure 4e-f). The
 378 isotopic variations of atmospheric water vapor in heavy rainfall events ($P = 68.4\text{-}141.1$ mm)
 379 were $37.4\text{-}66.8\text{‰}$ for $\delta^2\text{H}$, $3.41\text{-}5.70\text{‰}$ for $\delta^{18}\text{O}$, and $22.5\text{-}26.8\text{‰}$ for $d\text{-}excess$.



380

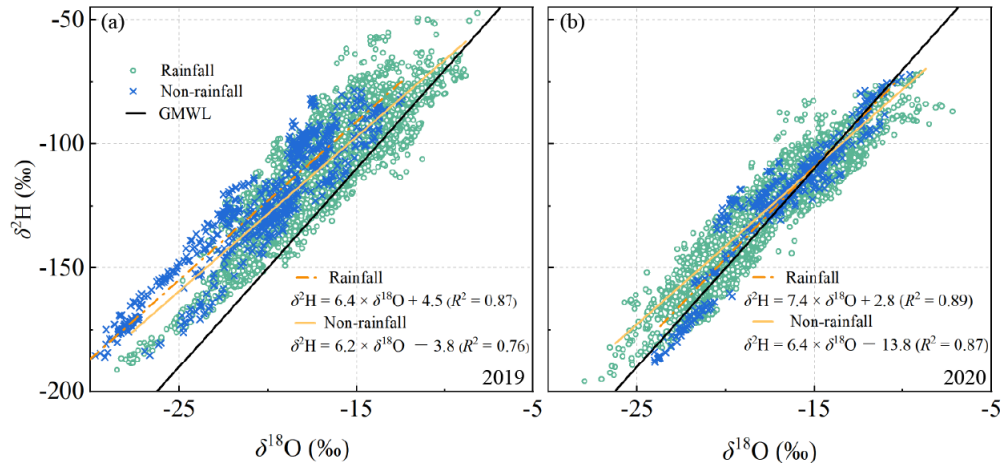
381 **Figure 4.** Impacts of rainfall processes on the diurnal cycles of atmospheric water vapor $\delta^2\text{H}$,
 382 $\delta^{18}\text{O}$, and $d\text{-}excess$ at 15 m height (a-f) during the (2019-2020) study periods. Rainfall amount
 383 (P) and rainfall duration (D) are plotted on each panel for reference. Shadow areas indicate the
 384 periods of rainfall events.

385

3.3 Relationships with meteorological variables

386

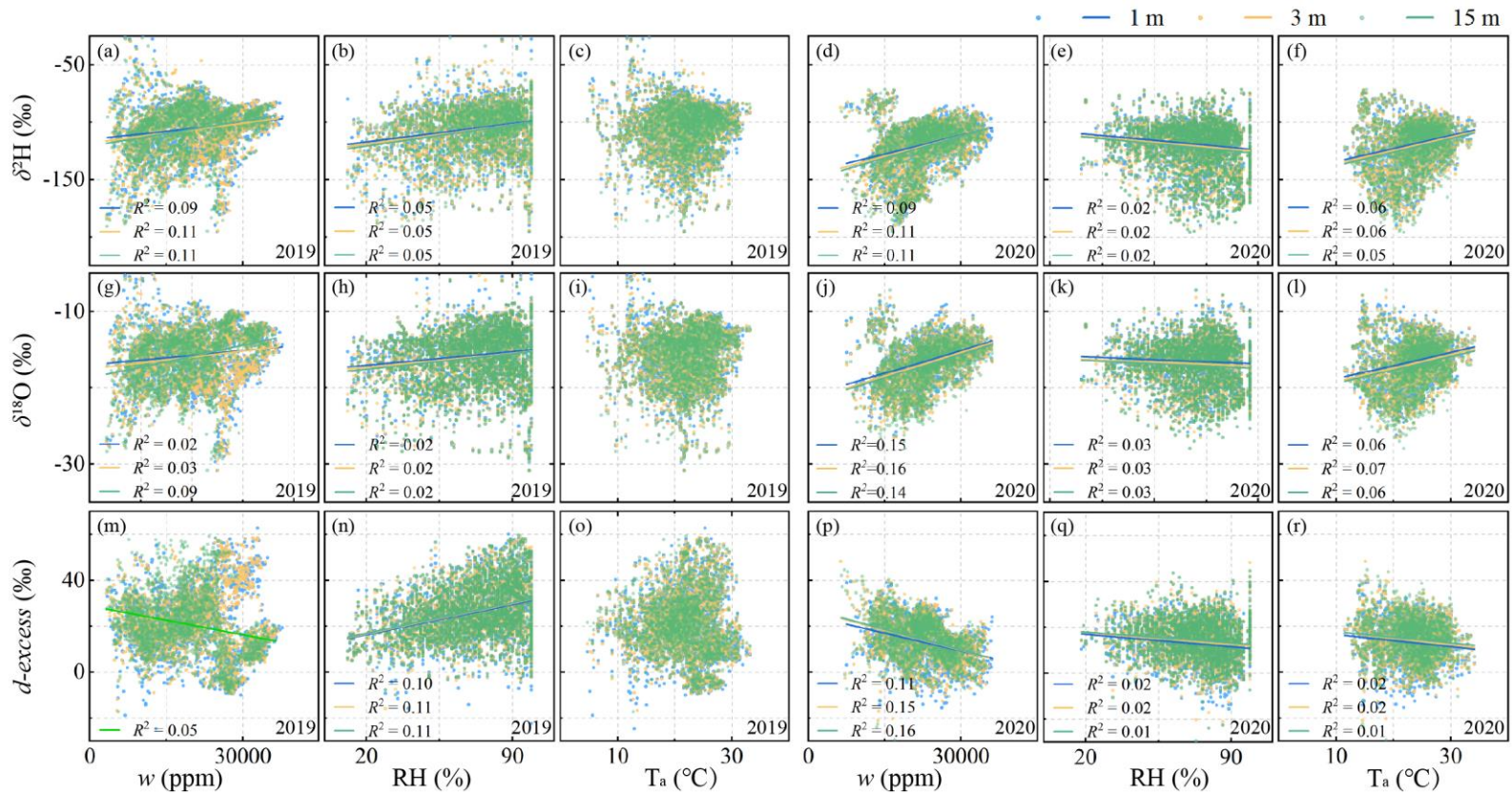
Figure 5 depicts the linear dependency of $\delta^2\text{H}$ on $\delta^{18}\text{O}$ for atmospheric water vapor
 387 during the 2019-2020 growing (May-September) seasons. The hourly measurement of three (i.e.,
 388 1 m, 3 m, and 15 m) canopy layers were merged to reflect the impacts of rainfall events on the
 389 co-variations between $\delta^2\text{H}$ on $\delta^{18}\text{O}$ of atmospheric water vapor. This treatment was adopted due
 390 to the similar functions among different heights (*SI Appendix A*, Figure S1). In 2019, the $\delta^2\text{H}$ and
 391 $\delta^{18}\text{O}$ of atmospheric water vapor mainly occupied the dual-isotope plots from the global meteoric
 392 water line (GMWL: $\delta^2\text{H} = 8 \times \delta^{18}\text{O} + 10$) to its left sides (Figure 5a). Slopes of the atmospheric
 393 water vapor lines in 2019 were 6.4 ± 0.2 ($R^2 = 0.87$, $P < 0.001$) and 6.2 ± 0.1 ($R^2 = 0.76$, $P <$
 394 0.001) during the rainfall and non-rainfall periods, respectively. In 2020, the $\delta^2\text{H}$ and $\delta^{18}\text{O}$ of
 395 atmospheric water vapor were plotted right on the GMWL (Figure 5b). Slopes of the
 396 atmospheric water vapor lines in 2020 were 7.4 ± 0.2 ($R^2 = 0.89$, $P < 0.001$) and 6.4 ± 0.1 ($R^2 =$
 397 0.87 , $P < 0.001$) during the rainfall and non-rainfall periods, respectively. The intercepts of the
 398 atmospheric water vapor lines were less than 10 for both years, ranging from 2.8 to 4.5 during
 399 the rainfall periods, and from -13.8 to -3.8 during the non-rainfall periods.



400

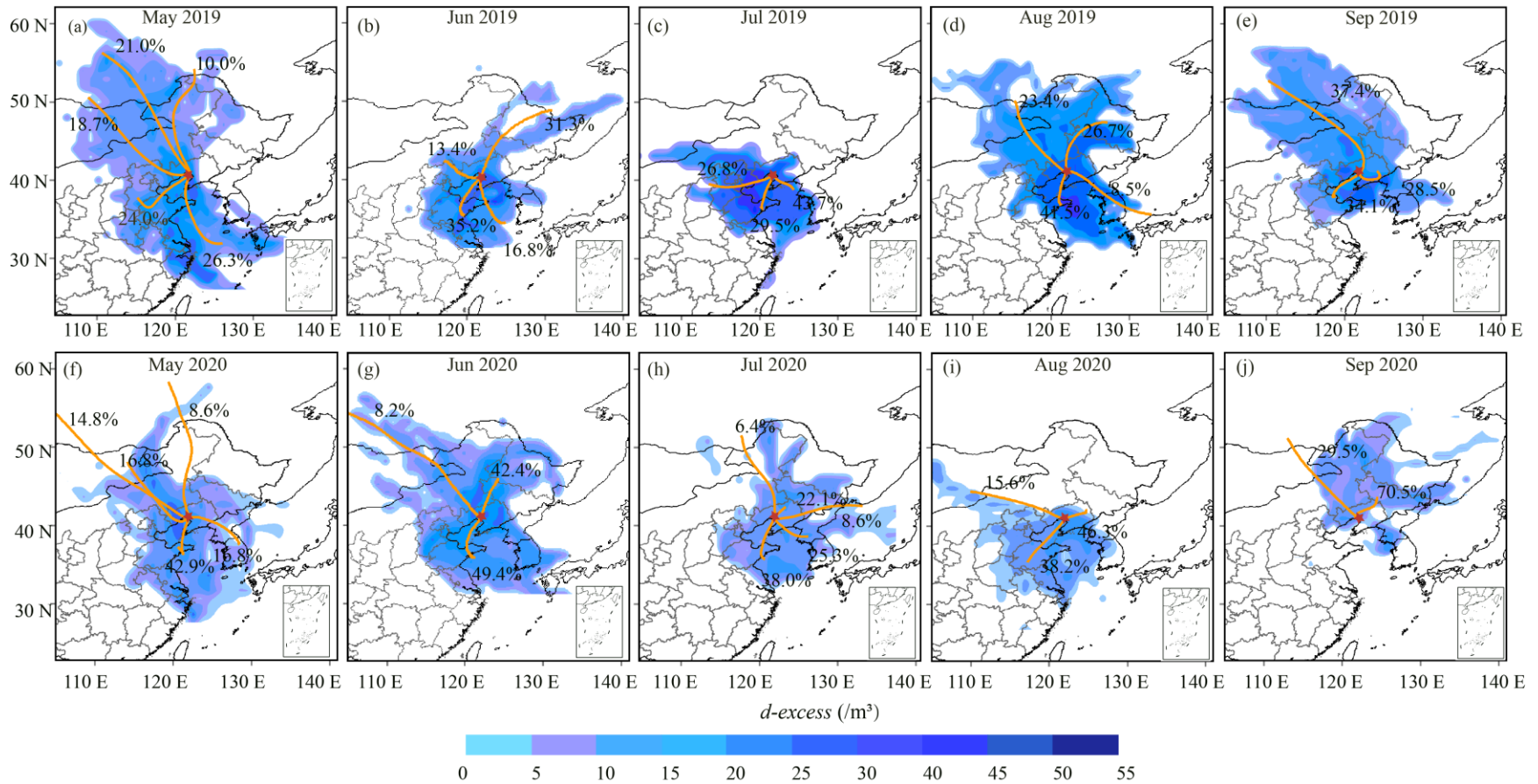
401 **Figure 5.** Isotopic values of $\delta^2\text{H}$ as a function of $\delta^{18}\text{O}$ in atmospheric water vapor during the
 402 2019 (a) and 2020 (b) growing (May-September) seasons. Data of atmospheric water vapor $\delta^2\text{H}$
 403 and $\delta^{18}\text{O}$ are divided into two groups representing the periods with rainfall and non-rainfall
 404 events. The global meteoric water line (GMWL: $\delta^2\text{H} = 8 \times \delta^{18}\text{O} + 10$) is also plotted on each
 405 panel for reference.

406 Figure 6 shows the relationships between the $\delta^2\text{H}$, $\delta^{18}\text{O}$ and d -excess of atmospheric
 407 water vapor and local meteorological factors. The $\delta^2\text{H}$ and $\delta^{18}\text{O}$ of atmospheric water vapor were
 408 positively correlated with the water vapor concentration (w) (Figure 6a, 6d, 6g, and 6j). In
 409 contrast, their d -excess were negatively correlated with w in 2019 ($R^2 = 0.05$, $P < 0.001$,
 410 measurement undertaken at height of 15 m, in Figure 6m) and 2020 ($R^2 = 0.11$ - 0.16 , $P < 0.001$,
 411 in Figure 6p). The atmospheric water vapor $\delta^2\text{H}$, $\delta^{18}\text{O}$ and d -excess were weakly dependent on
 412 the relative humidity (RH) during the study periods ($R^2 = 0.01$ - 0.11 , $P < 0.001$, in Figure 6b, 6e,
 413 6h, 6k, 6n, and 6q). The $\delta^2\text{H}$, $\delta^{18}\text{O}$ of atmospheric water vapor exhibited positive dependences on
 414 surface air temperature (T_a) in 2020 ($R^2 = 0.05$ - 0.07 , $P < 0.001$, in Figure 6f and 6l). The
 415 atmospheric water vapor d -excess in 2020 was negatively correlated with T_a ($R^2 = 0.01$ - 0.02 , $P <$
 416 0.001 , in Figure 6r). However, no significant correlation occurred between the atmospheric water
 417 vapor isotopes and T_a in 2019 (Figure 6c, 6i, and 6o).



418

419 **Figure 6.** Correlations of the water vapor concentration (w), relative humidity (RH), and surface air temperature (T_a) with the
 420 atmospheric water vapor $\delta^{2}\text{H}$ (a-f), $\delta^{18}\text{O}$ (g-l), and $d\text{-excess}$ (m-r) during the (2019-2020) study periods. The regression curves
 421 represent the in-situ atmospheric water vapor measurements at heights of 1 m (blue lines), 3 m (yellow lines), and 15 m (green lines).
 422



423
424
425
426
427

Figure 7. Back trajectory frequencies clustered according to the directions of air masses and the concentration fields of atmospheric water vapor d -excess during the 2019 (a-e) and 2020 (f-j) growing (May-September) seasons. Red star indicates the location of Panjin experimental station. Orange lines are the clusters of air masses during the preceding 48 h at 500 m height above the ground, and blue shading is the potential source of atmospheric water vapor d -excess in each month.

428 3.4 Large scale atmosphere circulations

429 Figure 7 shows the concentration fields of atmospheric water vapor *d-excess* along the
430 backward trajectories at Panjin experimental station. The 48-hourly backward trajectories of air
431 masses were calculated for the 2019-2020 growing (May-September) seasons. For all five
432 months, 3659 and 3515 trajectories were clustered in 2019 and 2020, respectively (*SI Appendix*
433 *A*, Figure S2). Then, we identified three-five major moisture source sectors that affected the
434 experimental station. The dominant air masses in this region generally came from ocean sources,
435 contributing more than 50% to the total air moisture except in June 2020 (49.4%). The transport
436 paths of ocean air masses could be further clustered into two sectors, i.e., Southwest-South (SW-
437 S) and South-Southeast (S-SE) directions. At the beginning of the monsoon season (May-June),
438 the trajectory paths of air masses usually originated from ocean surfaces and the northern interior
439 (Figure 7a-b and 7f-g). The ocean air masses gradually dominated during the peak monsoon
440 season (July-August). The contribution proportions of ocean air masses reached the maxima in
441 July 2019 (73.2%, in Figure 7c) and in August 2020 (84.5%, in Figure 7i). The influence of
442 summer monsoon on local air masses weakened in September 2019, with a contribution
443 proportion of 59.9% (Figure 7e). However, the ocean air masses had a prolonged impact (70.5%)
444 on atmospheric water vapor *d-excess* at the experimental station in September 2020 (Figure 7j).

445 The back-air mass trajectory analysis indicates that seasonal dynamic in moisture sources
446 was a main driving factor of the atmospheric water vapor *d-excess* variability (Figure 7). The
447 spatial distribution of atmospheric water vapor *d-excess* at this experimental station was closely
448 linked with the monsoon activities in East Asia. Most of trajectory paths were accompanied by
449 relatively higher atmospheric water vapor *d-excess* in 2019 than in 2020. This phenomenon was
450 particularly evident in 2019 (Figure 7a-e), where high-value of atmospheric water vapor *d-excess*
451 commonly distributed around the coastal regions. Lower proportion of air masses arose from the
452 ocean sources between August and September in 2019 (50-59.9%, in Figure 7d-e) than in 2020
453 (70.5-84.5%, in Figure 7i-j). However, the intensity of the East Asian monsoon was weak in
454 2020, which brought less rainfall to the atmospheric water cycles in Liaodong Bay. Therefore,
455 the air masses from the interiors of North China had more significant impacts (i.e., more negative
456 values) on the atmospheric water vapor *d-excess* in 2020 than in 2019. The secondary moisture
457 sources of inland air masses played a vital role in the seasonal variations of atmospheric water
458 vapor *d-excess* in the weak summer monsoon year.

459

460 **4 Discussion**

461 Based on the in-situ measurement techniques, this study revealed the isotopic signatures of
462 atmospheric water vapor (Figure 2-4), as well as the driving forces of the atmospheric water
463 vapor isotopes (Figure 5-7) for a reed wetland of Liaodong Bay, Northeast China. The
464 meteorological factors (e.g., water vapor concentration, relative humidity, and air temperature)
465 were incapable of predicting the variations of atmospheric water vapor $\delta^2\text{H}$, $\delta^{18}\text{O}$, and *d-excess*
466 in this region. The different seasonal and diurnal patterns of water vapor isotopes could be
467 attributed to the stronger monsoon activities in 2019 than in 2020. These findings would broaden
468 our understanding of hydrological cycles in the coastal wetlands.

469

4.1 Temporal dynamics of water vapor isotopes at different heights

470

471 The long- (i.e., seasonal scale) and short- (i.e., diurnal scale) term characteristics of
472 atmospheric water vapor isotopes showed significant variations at heights of 1 m, 3 m, and 15 m
473 (Figure 2 and 3). The temporal dynamics of water vapor $\delta^2\text{H}$, $\delta^{18}\text{O}$, and *d-excess* are usually
474 controlled by the atmospheric processes (Lee et al., 2005; Wen et al., 2008), local
475 evapotranspiration (Aron et al., 2019; Huang & Wen, 2014), and synoptic events (Berkelhammer
476 et al., 2013; Wu et al., 2019). For instance, Steen-Larsen et al. (2013) suggested that the intra-
477 seasonal variations of water vapor isotopes mainly result from the interplay between large-scale
478 moisture advection, boundary layer dynamics, and local moisture fluxes above the Greenland Ice
479 Sheet. The magnitude of changes in surface water vapor *d-excess* can be as high as 40‰ or
480 greater during several episodes (Steen-Larsen et al., 2013). Huang & Wen (2014) reported that
481 the atmospheric water vapor $\delta^2\text{H}$, $\delta^{18}\text{O}$, and *d-excess* are dominated by the typical arid and
482 continental climates, which will not show clear seasonal cycles in the inland region of Northwest
483 China. As a typical coastal wetland under the influence of the East Asian Monsoon, our results
484 showed that the temporal patterns of water vapor isotopes were strikingly different between the
485 years of study periods. Moreover, some departures of atmospheric water vapor isotopes were
486 observed among the three measurement heights. This might be interpreted as the enrichment
487 effects of local evapotranspiration, which gradually improves the atmospheric water vapor
isotopes with the increasing plant physiological activities (Hu et al., 2021; Welp et al., 2012).

488

The seasonal variations of atmospheric water vapor $\delta^2\text{H}$, $\delta^{18}\text{O}$, and *d-excess* in the reed
489 wetlands of Liaodong Bay were different from those of the other research site (Fiorella et al.,
490 2018; Laonamsai et al., 2021; Lee et al., 2006; Wen et al., 2010). Apart from the noticeable
491 seasonal changes occurring in each year, there were distinct inter-annual cycles for atmospheric
492 water vapor isotopes between 2019 and 2020 (Figure 2). The mean isotopic values of
493 atmospheric water vapor ranged from -120.7‰ to -108.4‰ for $\delta^2\text{H}$, from -16.98‰ to $-$
494 16.64‰ for $\delta^{18}\text{O}$, and from 13.3‰ to 26.3‰ (Table 1), which were higher than the results
495 reported by Wen et al. (2010) and Zhang et al. (2011) in inland areas of China. Especially in
496 2019, the $\delta^2\text{H}$ and $\delta^{18}\text{O}$ of atmospheric water vapor fluctuated seasonally with lower values in
497 the prevailing monsoon season (i.e., August-September). The seasonal pattern of atmospheric
498 water vapor $\delta^2\text{H}$ and $\delta^{18}\text{O}$ made a complete reversal of the water vapor concentration (*w*) trend
499 (Figure 2). In fact, the summer monsoon was earlier in 2019 and brought more rainfall than in
500 2020. In 2019, the typhoon “Lekima” was reported to land in Southwest coast of China (4-10
501 August) with a wind speed of 51.4 m s^{-1} , which then moved northwards and made a second
502 landfall in Liaodong Bay (Wang et al., 2021). Some studies reported that a significant decrease
503 in precipitation and atmospheric isotopes can happen during the tropical typhoons (Bonne et al.,
504 2019; Conroy et al., 2016). The abrupt decline of atmospheric water vapor *w* at 15 m height
505 could also be attributed to the high condensation efficiency and strong entrainment activity
506 during the typhoon event in 2019.

507

The interactions between atmospheric entrainment and local evapotranspiration typically
508 dominate the diurnal cycles of atmospheric water vapor $\delta^2\text{H}$, $\delta^{18}\text{O}$, and *d-excess* (Aron et al.,
509 2019; Huang & Wen, 2014; Lee et al., 2007; Zhao et al., 2014). Our results showed that the $\delta^2\text{H}$
510 and $\delta^{18}\text{O}$ of atmosphere were lower in the early morning (8:00-9:00 LST) than in the late
511 afternoon (16:00-18:00 LST). On the contrary, the atmospheric water vapor *d-excess* exhibited
512 an “inverted U-shaped diurnal pattern” in 2019 and 2020 (Figure 3). The downward trends in
513 atmospheric water vapor $\delta^2\text{H}$ and $\delta^{18}\text{O}$ can be attributed to the rapid increase of free air in ABL

514 when plant transpiration activity is relatively low in the morning (Huang & Wen, 2014). The
515 enrichment roles of local evapotranspiration surpassed the depletion effects of atmospheric
516 entrainment in the late afternoon. Such positive impacts of local evapotranspiration on
517 atmosphere isotopes were marked significantly in the lower (1 m) canopy than in the middle (3
518 m) and upper (15 m) heights (Figure 3). Apparently, the rainfall process was one of the main
519 factors contributing to the diurnal dynamics of atmospheric water vapor $\delta^2\text{H}$, $\delta^{18}\text{O}$, and *d-excess*
520 (Figure 4). The isotopic fractionation caused by the sub-cloud secondary evaporation enriches
521 the residual rainfall, which in turn can make the enrichment of atmospheric isotopes during small
522 rainfall events (Vuille et al., 2003; Wu et al., 2021). However, the rainout effects of rainfall
523 would result in the continuous depletion of atmospheric isotopes according to the Rayleigh
524 distillation mechanisms (Gat, 1996; Lee et al., 2005; Wen et al., 2010).

525 4.2 Controlling factors of water vapor isotopes above coastal wetlands

526 The global meteoric water line (GMWL: $\delta^2\text{H} = 8 \times \delta^{18}\text{O} + 10$) indicates the isotopic co-
527 variations in marine water that has not been exposed to evaporation fractionation (Craig, 1961;
528 Gat, 1996). As the marine air masses move over the coastal regions and towards the inland, the
529 air parcels will be mixed with continental water vapor sources and influenced by geographic
530 parameters such as the distances from coasts, altitudes, rainfall processes, and temperatures
531 (Christner et al., 2018; Gat, 1996; Merlivat & Jouzel, 1979). The slopes of atmospheric water
532 vapor lines (6.2-7.4) were lower than that of GMWL (Figure 5), which were determined by the
533 non-equilibrium fractionation (i.e., the existence of kinetic effects) within air parcels. Similarly,
534 Bastrikov et al. (2014) reported that the overall slopes of atmospheric water vapor lines are 5.6-
535 7.7 among different seasons in western Siberia (Kourovka). Li et al. (2020) highlighted that the
536 slopes of atmospheric water vapor lines change from 7.0 to 7.6 during a six-year period in
537 Eastern China. The high intercept (i.e., *d-excess*) of atmospheric water vapor lines in 2019
538 suggested that the isotopic changes in air masses which were very sensitive to the moisture
539 source conditions (Aemisegger et al., 2014; Delattre et al., 2015; Fiorella et al., 2018).

540 The results of this study also showed that the relationships between local meteorological
541 factors and atmospheric water vapor isotopes were weak or nonexistent at Panjin experimental
542 station (Figure 6). This finding was inconsistent with previous observations in the inland areas of
543 China. For example, Zhang et al. (2011) noted that the water vapor concentration (*w*) can be an
544 excellent predictor of atmospheric water vapor $\delta^2\text{H}$, $\delta^{18}\text{O}$, and *d-excess* based on the Rayleigh
545 distillation. However, the weak correlations between atmospheric water vapor isotopes and
546 relative humidity (RH) were found in other studies (Li et al., 2020; Salamalikis et al., 2015). An
547 earlier study by Lee et al. (2006) in New England found that the atmospheric *w* is a better
548 indicator for atmospheric water vapor isotopes than air temperature (T_a) on short time scales.
549 These studies have established a certain level of correlation between atmospheric water vapor
550 isotopes and local meteorological factors (e.g., *w*, T_a , and RH) during the non-monsoon season
551 (Lee et al., 2005; Li et al., 2020; Noone et al., 2012). In contrast, Wen et al. (2010) found that the
552 *w* becomes a poor predictor of the atmospheric water vapor $\delta^2\text{H}$, $\delta^{18}\text{O}$, and *d-excess* during the
553 summer monsoon season. Similar to this study, weak correlations were also found by Li et al.
554 (2020) and Wang et al. (2021) during the peak monsoon activities.

555 Unlike the $\delta^2\text{H}$ and $\delta^{18}\text{O}$ whose temporal variations are commonly overwhelmed by the
556 Rayleigh distillation and/or the rainout history of air masses, the atmospheric water vapor *d-*
557 *excess* of an air mass is a nearly constant tracer during the transport processes (Welp et al., 2012;

558 Wei et al., 2019). Therefore, the *d-excess* of atmospheric water vapor is widely used as a
559 conservative indicator for identifying the moisture source locations (Aemisegger et al., 2014;
560 Steen-Larsen et al., 2015; Uemura et al., 2008; Xu et al., 2022). Panjin experimental station was
561 situated on the special borderland between the North China Plain and Bohai Sea (Figure 1),
562 which was also located within the edge of the East Asian monsoon region (Luo et al., 2021;
563 Wang et al., 2021). With the sea in three directions, the atmospheric water vapor *d-excess* in this
564 study was significantly affected by the ocean air masses (Figure 7). The high values of
565 atmospheric water vapor *d-excess* consistently appeared in the peak (i.e., July-August) monsoon
566 season. The results of the present study further confirmed that the ocean air masses dominated
567 the temporal variations of atmospheric water vapor *d-excess* (Figures 2, 3, and 7) when a super
568 typhoon “Lekima” happened in 2019 (details in Section 4.1). Lai et al. (2018) examined the
569 atmospheric water cycling above a coastal mangrove forest in Southern China. They also found
570 that the substantial increase of atmospheric water vapor *d-excess* is related to the passage of a
571 tropical typhoon “Talas” (Lai et al., 2018). In the Qinghai-Tibetan Plateau of central Asia, Wu et
572 al. (2019) revealed that high *d-excess* values of atmospheric water vapor were influenced by
573 local moisture mixing during the monsoon season. A recent study noted that high values of
574 atmospheric water vapor *d-excess* appear before the monsoon onset and after the monsoon
575 season at Lhasa in Southern Tibetan Plateau (Tian et al., 2020). Indeed, air masses from cold and
576 dry areas can also bring a relatively high atmospheric water vapor *d-excess* (Uemura et al., 2008;
577 Xu et al., 2022). Further mechanism studies are expected to provide more rational explanations
578 for the above-mentioned processes in coastal wetlands.

579

580 **5 Conclusions**

581 The inter-annual variations of atmospheric water vapor $\delta^2\text{H}$, $\delta^{18}\text{O}$, and *d-excess* were
582 significantly different between 2019 and 2020. On a seasonal time scale, the mean isotopic
583 values of atmospheric water vapor in 2019 were significantly higher than that in 2020.
584 Meanwhile, the $\delta^2\text{H}$ and $\delta^{18}\text{O}$ of atmospheric water vapor gradually decreased from the lower (1
585 m), to the middle (3 m) and upper (15 m) canopy both 2019 and 2020. A clear diurnal cycle of
586 atmospheric water vapor isotopes existed during the study periods, which was more pronounced
587 in 2019 than in 2020. The diurnal isotopic differences of atmospheric water vapor among
588 measurement heights (i.e., 1, 3, and 15 m) were more evident in the daytime (8:00-20:00 LST)
589 than at night (20:00-8:00 LST). Rainfall events had a significant impact on the diurnal dynamics
590 of atmospheric water vapor $\delta^2\text{H}$, $\delta^{18}\text{O}$, and *d-excess*, depending on the rainfall intensity (i.e.,
591 amount and duration). The correlations between atmospheric water vapor isotopes and local
592 meteorological factors were weak or nonexistent in the study region. Instead, the spatial-
593 temporal dynamics of atmospheric water vapor isotopes were highly consistent with the
594 monsoon activities. The moisture in air masses could be clustered into three to-five primary
595 sources, with over 60% from the ocean sources. High *d-excess* values reflected the
596 predominating influences of ocean air masses on atmospheric water vapor cycles in the coastal
597 regions.

598

599 **Acknowledgments**

600 We are deeply thankful to Ye Zhang, Long Chen, Xian-zhe Liu, and Han Wang (Panjin National
601 Climatic Observatory, Institute of Atmospheric Environment, China Meteorological
602 Administration) for field support. We would like to extend our thanks to Institutional Center for
603 Shared Technologies and Facilities of Xishuangbanna Tropical Botanical Garden, Chinese
604 Academy of Sciences for laboratory process support. We also acknowledge the NOAA-Air
605 Resources Laboratory (ARL) for providing the HYSPLIT model and meteorological data. This
606 research was supported by the National Natural Science Foundation of China [32171557,
607 32171529], the Yunnan Natural Science Foundation [202201AT070221], the Youth Innovation
608 Promotion Association of Chinese Academy of Sciences [2021397], the National Science and
609 Technology Basic Resources Survey Program of China [2019FY0101302], the National Key
610 R&D Program of China [2022YFF0801301], the Key Project of Liaoning Provincial
611 Meteorological Bureau [LNCP202205].

612

613 **Open Research**

614 Data for this study consist of water isotopes and environmental variables that are available at
615 <https://doi.org/10.11888/Atmos.tpd.272899>

616

617 **References**

- 618 Aemisegger, F., Pfahl, S., Sodemann, H., Lehner, I., Seneviratne, S. I., & Wernli, H. (2014).
619 Deuterium excess as a proxy for continental moisture recycling and plant transpiration.
620 *Atmospheric Chemistry and Physics*, 14(8), 4029-4054. [https://doi.org/10.5194/acp-14-](https://doi.org/10.5194/acp-14-4029-2014)
621 [4029-2014](https://doi.org/10.5194/acp-14-4029-2014)
- 622 Araguas-Araguas, L., Froehlich, K., Rozanski, K. (2000). Deuterium and oxygen-18 isotope
623 composition of precipitation and atmospheric moisture. *Hydrological Processes*, 14(8),
624 1341-1355. [https://doi.org/10.1002/1099-1085\(20000615\)14:8<1341::Aid-](https://doi.org/10.1002/1099-1085(20000615)14:8<1341::Aid-hyp983>3.0.Co;2-z)
625 [hyp983>3.0.Co;2-z](https://doi.org/10.1002/1099-1085(20000615)14:8<1341::Aid-hyp983>3.0.Co;2-z)
- 626 Aron, P. G., Poulsen, C.J., Fiorella, R. P., & Matheny, A. M. (2019). Stable water isotopes reveal
627 effects of intermediate disturbance and canopy structure on forest water cycling. *Journal of*
628 *Geophysical Research: Biogeosciences*, 124(10), 2958-2975.
629 <https://doi.org/10.1029/2019jg005118>
- 630 Bagheri, R., Bagheri, F., Karami, G. H., & Jafari, H. (2019). Chemo-isotopes (^{18}O & ^2H)
631 signatures and HYSPLIT model application: Clues to the atmospheric moisture and air mass
632 origins. *Atmospheric Environment*, 215, 116892.
633 <https://doi.org/10.1016/j.atmosenv.2019.116892>
- 634 Bailey, A., Noone, D., Berkelhammer, M., Steen-Larsen, H. C., & Sato, P. (2015). The stability
635 and calibration of water vapor isotope ratio measurements during long-term deployments.
636 *Atmospheric Measurement Techniques*, 4521-4538. [https://doi.org/10.5194/amt-8-4521-](https://doi.org/10.5194/amt-8-4521-2015)
637 [2015](https://doi.org/10.5194/amt-8-4521-2015)
- 638 Bastrikov, V., Steen-Larsen, H. C., Masson-Delmotte, V., Griбанov, K., Cattani, O., Jouzel, J., &
639 Zakharov, V. (2014). Continuous measurements of atmospheric water vapour isotopes in

- 640 western Siberia (Kourovka). *Atmospheric Measurement Techniques*, 7(6), 1763-1776.
641 <https://doi.org/10.5194/amt-7-1763-2014>
- 642 Berkelhammer, M., Hu, J., Bailey, A., Noone, D. C., Still, C. J., Barnard, H., et al. (2013). The
643 nocturnal water cycle in an open-canopy forest. *Journal of Geophysical Research:*
644 *Atmospheres*, 118(17), 10225-10242. <https://doi.org/10.1002/jgrd.50701>
- 645 Bonne, J. L., Behrens, M., Meyer, H., Kipfstuhl, S., Rabe, B., Schönicke, L., et al. (2019).
646 Resolving the controls of water vapour isotopes in the Atlantic sector. *Nature*
647 *Communications*, 10(1), 1-10. <https://doi.org/10.1038/s41467-019-09242-6>
- 648 Bonne, J. L., Meyer, H., Behrens, M., Boike, J., Kipfstuhl, S., Rabe, B. et al. (2020). Moisture
649 origin as a driver of temporal variabilities of the water vapour isotopic composition in the
650 Lena River Delta, Siberia. *Atmospheric Chemistry and Physics*, 20(17), 10493-10511.
651 <https://doi.org/10.5194/acp-20-10493-2020>
- 652 Casado, M., Cauquoin, A., Masson-Delmotte, V., Genthon, C., Kerstel, E., Kassi, S., et al.
653 (2016). Continuous measurements of isotopic composition of water vapour on the East
654 Antarctic Plateau. *Atmospheric Chemistry and Physics*, 16(13), 8521-8538.
655 <https://doi.org/10.5194/acp-16-8521-2016>
- 656 Christner, E., Aemisegger, F., Pfahl, S., Werner, M., Cauquoin, A., Schneider, M. et al. (2018).
657 The climatological impacts of continental surface evaporation, rainout, and subcloud
658 processes on δD of water vapor and precipitation in Europe. *Journal of Geophysical*
659 *Research: Atmospheres*, 123(8), 4390-4409. <https://doi.org/10.1002/2017jd027260>
- 660 Christner, E., Kohler, M., & Schneider, M. (2017). The influence of snow sublimation and
661 meltwater evaporation on δD of water vapor in the atmospheric boundary layer of central

- 662 Europe. *Atmospheric Chemistry and Physics*, 17(2), 1207-1225.
663 <https://doi.org/10.5194/acp-17-1207-2017>
- 664 Conroy, J. L., Noone, D., Cobb, M. K., Moerman, J. W., & Konecky, B. L. (2016). Paired stable
665 isotopologues in precipitation and vapor: A case study of the amount effect within western
666 tropical Pacific storms. *Journal of Geophysical Research: Atmospheres*, 121(7), 3290-3303.
667 <https://doi.org/10.1002/2015jd023844>
- 668 Craig, H. (1961). Isotopic variations in meteoric waters. *Science*, 133(346), 1702-1703.
669 <https://doi.org/10.1126/science.133.3465.1702>
- 670 Cui, J. P., Tian, L. D., & Gibson, J. J. (2018). When to conduct an isotopic survey for lake water
671 balance evaluation in highly seasonal climates. *Hydrological Processes*, 32(3), 379-387.
672 <https://doi.org/10.1002/hyp.11420>
- 673 Dahinden, F., Aemisegger, F., Wernli, H., Schneider, M., Diekmann, C.J., Ertl, B., et al. (2021).
674 Disentangling different moisture transport pathways over the eastern subtropical North
675 Atlantic using multi-platform isotope observations and high-resolution numerical
676 modelling. *Atmospheric Chemistry and Physics*, 21(21), 16319-16347.
677 <https://doi.org/10.5194/acp-21-16319-2021>
- 678 Dansgaard W. (1964). Stable isotopes in precipitation. *Tellus*, 16(4): 436-468.
679 <https://doi.org/10.3402/tellusa.v16i4.8993>
- 680 Delattre, H., Vallet-Coulomb C., & Sonzogni, C. (2015). Deuterium excess in the atmospheric
681 water vapour of a Mediterranean coastal wetland: regional vs. local signatures. *Atmospheric
682 Chemistry and Physics*, 15(17), 10167-10181. <https://doi.org/10.5194/acp-15-10167-2015>

- 683 Devi, P., Jain, A. K., Rao, M. S., & Kumar B. (2014). Experimental study on isotope
684 fractionation of evaporating water of different initial isotopic composition. *Journal of*
685 *Radioanalytical and Nuclear Chemistry*, 302(2), <https://doi.org/10.1007/s10967-014-3368-7>
- 686 Diekmann, C. J., Schneider, M., Knippertz, P., Vries, A. J., Pfahl, S., Aemisegger, F., et al.
687 (2021). A lagrangian perspective on stable water isotopes during the West African
688 Monsoon. *Journal of Geophysical Research: Atmospheres*, 126(19), e2021JD034895.
689 <https://doi.org/10.1029/2021jd034895>
- 690 Farlin, J., Lai, C. T., & Yoshimura, K. (2013). Influence of synoptic weather events on the
691 isotopic composition of atmospheric moisture in a coastal city of the western United States.
692 *Water Resources Research*, 49(6), 3685-3696. <https://doi.org/10.1002/wrcr.20305>
- 693 Fiorella, R. P., Poulsen, C. J. & Matheny, A. M. (2018). Seasonal patterns of water cycling in a
694 deep, continental mountain valley inferred from stable water vapor isotopes. *Journal of*
695 *Geophysical Research: Atmospheres*, 123(14), 7271-7291.
696 <https://doi.org/10.1029/2017jd028093>
- 697 Fiorella, R. P., West, J. B., & Bowen, G. J. (2019). Biased estimates of the isotope ratios of
698 steady-state evaporation from the assumption of equilibrium between vapour and
699 precipitation. *Hydrological Processes*, 33(19), 2576-2590.
700 <https://doi.org/10.1002/hyp.13531>
- 701 Galewsky, J., Jensen, M. P., & Delp, J. (2022). Marine boundary layer decoupling and the stable
702 isotopic composition of water vapor. *Journal of Geophysical Research: Atmospheres*,
703 127(3), e2021JD035470. <https://doi.org/10.1029/2021jd035470>

- 704 Galewsky, J., Rella, C., Sharp, Z., Samuels, K., & Ward, D. (2011). Surface measurements of
705 upper tropospheric water vapor isotopic composition on the Chajnantor Plateau, Chile.
706 *Geophysical Research Letters*, 38(17), L17803. <https://doi.org/10.1029/2011gl048557>
- 707 Galewsky, J. Steen-Larsen, H. C., Field, R. D., Worden, J., Risi, C., & Schneider, M. (2016).
708 Stable isotopes in atmospheric water vapor and applications to the hydrologic cycle.
709 *Reviews of Geophysics*, 54(4), 809-865. <https://doi.org/10.1002/2015rg000512>
- 710 Gat, J. R. (1996). Oxygen and hydrogen isotopes in the hydrologic cycle. *Annual Review of*
711 *Earth and Planetary Sciences*, 24, 225-262. <https://doi.org/10.1146/annurev.earth.24.1.225>
- 712 Gonzalez, Y., Schneider, M., Rodriguez, S., Christner, E., Garcia, O. E., Cuevas, E., et al.
713 (2016). Detecting moisture transport pathways to the subtropical North Atlantic free
714 troposphere using paired H₂O- δ D in situ measurements. *Atmospheric Chemistry and*
715 *Physics*, 16(7), 4251-4269. <https://doi.org/10.5194/acp-16-4251-2016>
- 716 Griffis, T. J., Wood, J. D., Baker, J. M., Lee, X. H., Xiao, K., Chen, Z. C., et al. (2016).
717 Investigating the source, transport, and isotope composition of water vapor in the planetary
718 boundary layer. *Atmospheric Chemistry and Physics*, 16(8), 5139-5157.
719 <https://doi.org/10.5194/acp-16-5139-2016>
- 720 Hu, Y. B., Xiao, W., Wei, Z. W., Welp, L. R., Wen, X. F., & Lee, X. H. (2021). Determining the
721 isotopic composition of surface water vapor flux from high-frequency observations using
722 flux-gradient and keeling plot methods. *Earth and Space Science*, 8(3), e2020EA001304.
723 <https://doi.org/10.1029/2020ea001304>
- 724 Hu, Z. M., Wen, X. F., Sun, X. M., Li, L. H., Yu, G. R., Lee, X. H. & Li S. G. (2014).
725 Partitioning of evapotranspiration through oxygen isotopic measurements of water pools

- 726 and fluxes in a temperate grassland. *Journal of Geophysical Research: Biogeosciences*,
727 *119*(3), 358-371. <https://doi.org/10.1002/2013jg002367>
- 728 Huang, L. J., & Wen, X F. (2014). Temporal variations of atmospheric water vapor δD and $\delta^{18}O$
729 above an arid artificial oasis cropland in the Heihe River Basin. *Journal of Geophysical*
730 *Research: Atmospheres*, *119*(19), 11456-11476. <https://doi.org/10.1002/2014jd021891>
- 731 Huang, Y. Y., Wang, B., Li, X. F., & Wang, H. J. (2018). Changes in the influence of the
732 western Pacific subtropical high on Asian summer monsoon rainfall in the late 1990s.
733 *Climate Dynamics*, *51*(1-2), 443-455. <https://doi.org/10.1007/s00382-017-3933-1>
- 734 Kurita, N., Newman, B. D., Araguas-Araguas, L. J., & Aggarwal, P. (2012). Evaluation of
735 continuous water vapor δD and $\delta^{18}O$ measurements by off-axis integrated cavity output
736 spectroscopy. *Atmospheric Measurement Techniques*, *5*(8), 2069-2080.
737 <https://doi.org/10.5194/amt-5-2069-2012>
- 738 Lai, C.T., & Ehleringer, J. (2011). Deuterium excess reveals diurnal sources of water vapor in
739 forest air. *Oecologia*, *165*(1), 213-223. <https://doi.org/10.1007/s00442-010-1721-2>
- 740 Lai, X., Wright, J. S., Huang, W. Y., Liang, J., Lin, G. H., & Zhu, S. X. (2018). Contributions of
741 atmospheric transport and rain-vapor exchange to near-surface water vapor in the Zhanjiang
742 Mangrove Reserve, southern China: an isotopic perspective. *Atmosphere*, *9*(9), 365.
743 <https://doi.org/10.3390/atmos9090365>
- 744 Laonamsai, J., Ichiyanagi, K., Patsinghasanee, S., & Kamdee, K. (2021). Controls on stable
745 isotopic characteristics of water vapour over Thailand. *Hydrological Processes*, *35*(7),
746 e14202. <https://doi.org/10.1002/hyp.14202>

- 747 Lee, X. H., Sargent, S., Smith, R., & Tanner, B. (2005). In situ measurement of the water vapor
748 $^{18}\text{O}/^{16}\text{O}$ isotope ratio for atmospheric and ecological applications. *Journal of Atmospheric
749 and Oceanic Technology*, 22(8), 1305-1305. <https://doi.org/10.1175/JTECH9001.1a>
- 750 Lee, X. H., Smith, R., & Williams, J. (2006). Water vapour $^{18}\text{O}/^{16}\text{O}$ isotope ratio in surface air in
751 New England, USA. *Tellus Series B-Chemical and Physical Meteorology*, 58(4), 293-304.
752 <https://doi.org/10.1111/j.1600-0889.2006.00191.x>
- 753 Lee, X. H., Kim, K., & Smith R. (2007). Temporal variations of the $^{18}\text{O}/^{16}\text{O}$ signal of the whole-
754 canopy transpiration in a temperate forest. *Global Biogeochemical Cycles*, 21, GB3013.
755 <https://doi.org/10.1029/2006gb002871>
- 756 Li, Y. J., An, W. L., Pang, H. X., Wu, S. Y., Tang, Y. Y., Zhang, W. B., & Hou, S.G. (2020).
757 Variations of stable isotopic composition in atmospheric water vapor and their controlling
758 factors-a 6-year continuous sampling study in Nanjing, eastern China. *Journal of
759 Geophysical Research: Atmospheres*, 125, e2019JD031697.
760 <https://doi.org/10.1029/2019jd031697>
- 761 Luo, J. S., Sun, Y. H., Wang, Y. G., Xie, Z. H., & Meng, L. D. (2021). Cenozoic tectonic
762 evolution of the eastern Liaodong Bay sub-basin, Bohai Bay basin, eastern China-
763 Constraints from seismic data. *Marine and Petroleum Geology*, 134, 105346.
764 <https://doi.org/10.1016/j.marpetgeo.2021.105346>
- 765 Mao, D.H., He, X.Y., Wang, Z.M., Tian, Y.L., Xiang, H.X., Yu, H., et al. (2019). Diverse
766 policies leading to contrasting impacts on land cover and ecosystem services in Northeast
767 China. *Journal of Cleaner Production*, 240, 117961.
768 <https://doi.org/10.1016/j.jclepro.2019.117961>

- 769 Mao, D.H., Wang, Z.M., Du, B.J., Li, L., Tian, Y.L., Zeng, Y., et al. (2020). National wetland
770 mapping in China: A new product resulting from object based and hierarchical classification
771 of Landsat 8 OLI images. *ISPRS Journal of Photogrammetry and Remote Sensing*, 164, 11-
772 25 <https://doi.org/10.1016/j.isprsjprs.2020.03.020>
- 773 Mercer, J. J., Liefert, D. T., & Williams, D. G. (2020). Atmospheric vapour and precipitation are
774 not in isotopic equilibrium in a continental mountain environment. *Hydrological Processes*,
775 34(14), 3078-3101. <https://doi.org/10.1002/hyp.13775>
- 776 Merlivat, L., & Jouzel, J. (1979). Global climatic interperetation of the deuterium ¹⁸O
777 relationship for precipitation. *Journal of Geophysical Research: Oceans*, 84(C8), 5029-
778 5033. <https://doi.org/10.1029/jc084ic08p05029>
- 779 Munksgaard, N. C., Zwart, C., Haig, J., Cernusak, L. A., & Bird, M. I. (2020). Coupled rainfall
780 and water vapour stable isotope time series reveal tropical atmospheric processes on
781 multiple timescales. *Hydrological Processes*, 34(1), 111-124.
782 <https://doi.org/10.1002/hyp.13576>
- 783 NFGA. (2010). National Wetland Survey Statistics Report. National Forestrty and Grassland
784 Administration (in Chinese). <https://www.forestry.gov.cn>
- 785 Noone, D. (2012). Pairing measurements of the water vapor isotope ratio with humidity to
786 deduce atmospheric moistening and dehydration in the tropical midtroposphere. *Journal of*
787 *Climate*, 25(13), 4476-4494. <https://doi.org/10.1175/jcli-d-11-00582.1>
- 788 Parkes, S. D., McCabe, M. F., Griffiths, A. D., Wang, L. X., Chambers, S., Ershadi, A., et al.
789 (2017). Response of water vapour *D-excess* to land-atmosphere interactions in a semi-arid
790 environment. *Hydrology and Earth System Sciences*, 21(1), 533-548.
791 <https://doi.org/10.5194/hess-21-533-2017>

- 792 Salamalikis, V., Argiriou, A. A., & Dotsika, E. (2015). Stable isotopic composition of
793 atmospheric water vapor in Patras, Greece: a concentration weighted trajectory approach.
794 *Atmospheric Research*, 152, 93-104. <https://doi.org/10.1016/j.atmosres.2014.02.021>
- 795 Steen-Larsen, H. C., Johnsen, S. J., Masson-Delmotte, V., Stenni, B., Risi, C., Sodemann, H., et
796 al. (2013). Continuous monitoring of summer surface water vapor isotopic composition
797 above the Greenland Ice Sheet. *Atmospheric Chemistry and Physics*, 13(9), 4815-4828.
798 <https://doi.org/10.5194/acp-13-4815-2013>
- 799 Steen-Larsen, H. C., Masson-Delmotte, V., Hirabayashi, M., Winkler, R., Satow, K., Prie, F., et
800 al. (2014b). What controls the isotopic composition of Greenland surface snow? *Climate of*
801 *the Past*, 10(1), 377-392. <https://doi.org/10.5194/cp-10-377-2014>
- 802 Steen-Larsen, H. C., Sveinbjörnsdóttir, A. E., Jonsson, T., Ritter, F., Bonne, J. L., Masson-
803 Delmotte, V., et al. (2015). Moisture sources and synoptic to seasonal variability of North
804 Atlantic water vapor isotopic composition. *Journal of Geophysical Research: Atmospheres*,
805 120(12), 5757-5774. <https://doi.org/10.1002/2015jd023234>
- 806 Steen-Larsen, H. C., Sveinbjörnsdóttir, A. E., Peters, A. J., Masson-Delmotte, V., Guishard, M.
807 P., Hsiao, G., et al. (2014a). Climatic controls on water vapor deuterium excess in the
808 marine boundary layer of the North Atlantic based on 500 days of in situ, continuous
809 measurements. *Atmospheric Chemistry and Physics*, 14(15), 7741-7756.
810 <https://doi.org/10.5194/acp-14-7741-2014>
- 811 Sturm, P., & Knohl, A. (2010). Water vapor $\delta^2\text{H}$ and $\delta^{18}\text{O}$ measurements using off-axis
812 integrated cavity output spectroscopy. *Atmospheric Measurement Techniques*, 3(1), 67-77.
813 <https://doi.org/10.5194/amt-3-67-2010>

- 814 Tian, L. D., Yu, W. S., Schuster, P. F., Wen, R., Cai, Z. Y., Wang, D., et al. (2020). Control of
815 seasonal water vapor isotope variations at Lhasa, southern Tibetan Plateau. *Journal of*
816 *Hydrology*, 580, 124237. <https://doi.org/10.1016/j.jhydrol.2019.124237>
- 817 Tremoy, G., Vimeux, F., Vimeux, F., Souley, I., Risi, C., Favreau, G., & Oi, M. (2014).
818 Clustering mesoscale convective systems with laser-based water vapor delta O-18
819 monitoring in Niamey (Niger). *Journal of Geophysical Research: Atmospheres*, 119(9),
820 5079-5103. <https://doi.org/10.1002/2013jd020968>
- 821 Uemura, R., Matsui, Y., Yoshimura, K., Motoyama, H., & Yoshida, N. (2008). Evidence of
822 deuterium excess in water vapor as an indicator of ocean surface conditions. *Journal of*
823 *Geophysical Research: Atmospheres*, 113, D19114. <https://doi.org/10.1029/2008jd010209>
- 824 Vuille, M., Bradley, R. S., Werner, M., Healy, R., & Keimig, F. (2003). Modeling $\delta^{18}\text{O}$ in
825 precipitation over the tropical Americas: interannual variability and climatic controls.
826 *Journal of Geophysical Research: Atmospheres*, 108(D6), 4174.
827 <https://doi.org/10.1029/2001jd002038>
- 828 Wang, G. D., Wang, M., Lu, X. G., & Jiang, M. (2016). Surface elevation change and
829 susceptibility of coastal wetlands to sea level rise in Liaohe Delta, China. *Estuarine Coastal*
830 *and Shelf Science*, 180, 204-211. <https://doi.org/10.1016/j.ecss.2016.07.011>
- 831 Wang, G. Y., Lan, H. M., & Liu, Z. F. (2021). Stable isotope record of super typhoon Lekima
832 (2019). *Atmospheric Research*, 264, 264, 105822.
833 <https://doi.org/10.1016/j.atmosres.2021.105822>
- 834 Wei, Z. W., & Lee, X. H. (2019). The utility of near-surface water vapor deuterium excess as an
835 indicator of atmospheric moisture source. *Journal of Hydrology*, 577, 123923.
836 <https://doi.org/10.1016/j.jhydrol.2019.123923>

- 837 Wei, Z. W., Yoshimura, K., Okazaki, A., Kim, W., Liu, Z. F., & Yokoi, M. (2015). Partitioning
838 of evapotranspiration using high-frequency water vapor isotopic measurement over a rice
839 paddy field. *Water Resources Research*, 51(5), 3716-3729.
840 <https://doi.org/10.1002/2014wr016737>
- 841 Welp, L. R., Lee, X. H., Griffis, T. J., Wen, X. F., Xiao, W., Li, S. G., et al. (2012). A meta-
842 analysis of water vapor deuterium-excess in the midlatitude atmospheric surface layer.
843 *Global Biogeochemical Cycles*, 26, GB3021. <https://doi.org/10.1029/2011gb004246>
- 844 Wen, X. F., Lee, X. H., Sun, X. M., Wang, J. L., Hu, Z. M., Li, S.G., & Yu, G.R. (2012). Dew
845 water isotopic ratios and their relationships to ecosystem water pools and fluxes in a
846 cropland and a grassland in China. *Oecologia*, 168(2), 549-561.
847 <https://doi.org/10.1007/s00442-011-2091-0>
- 848 Wen, X. F., Sun, X. M., Zhang, S. C., Yu, G. R., Sargent, S. D., & Lee, X. H. (2008).
849 Continuous measurement of water vapor D/H and $^{18}\text{O}/^{16}\text{O}$ isotope ratios in the atmosphere.
850 *Journal of Hydrology*, 349(3-4), 489-500. <https://doi.org/10.1016/j.jhydrol.2007.11.021>
- 851 Wen, X. F., Zhang, S. C., Sun, X. M., Yu, G. R., & Lee, X. H. (2010). Water vapor and
852 precipitation isotope ratios in Beijing, China. *Journal of Geophysical Research:*
853 *Atmospheres*, 115, D1103. <https://doi.org/10.1029/2009jd012408>
- 854 Wu, H. W, Li, X. Y., Zhang, J. M., Li, J., Liu, J. Z., Tian, L. H., & Fu, C.S. (2019). Stable
855 isotopes of atmospheric water vapour and precipitation in the northeast Qinghai-Tibetan
856 Plateau. *Hydrological Processes*, 33(23), 2997-3009. <https://doi.org/10.1002/hyp.13541>
- 857 Wu, X. X., Chen, F. L., Liu, X. Y, Wang, S. J., Zhang, M. J., Zhu, G. F., et al. (2021). The
858 significance of hydrogen and oxygen stable isotopes in the water vapor source in Dingxi
859 area. *Water*, 13(17), 2374. <https://doi.org/10.3390/w13172374>

- 860 Xiao, W., Lee, X. H., Hu, Y. B., Liu, S. D., Wang, W., Wen, X. F., et al. (2017). An
861 experimental investigation of kinetic fractionation of open-water evaporation over a large
862 lake. *Journal of Geophysical Research: Atmospheres*, 122(21), 11651-11663.
863 <https://doi.org/10.1002/2017jd026774>
- 864 Xu, T., Pang, H. X., Zhan, Z. J., Zhang, W. B., Guo, H. W., Wu, S. Y., & Hou, S. G. (2022).
865 Water vapor isotopes indicating rapid shift among multiple moisture sources for the 2018-
866 2019 winter extreme precipitation events in southeastern China. *Hydrology and Earth
867 System Sciences*, 26(1), 117-127. <https://doi.org/10.5194/hess-26-117-2022>
- 868 Zhang, S. C., Sun X. M., Wang J. L., Yu, G. R., Wen, X. F. (2011). Short-term variations of
869 vapor isotope ratios reveal the influence of atmospheric processes. *Journal of Geographical
870 Sciences*, 21(3), 401-416. <https://doi.org/10.1007/s11442-011-0853-6>
- 871 Zhao, L., Wang, L., Liu, X., Xiao, H., Ruan, Y., & Zhou, M. (2014). The patterns and
872 implications of diurnal variations in the d-excess of plant water, shallow soil water and air
873 moisture. *Hydrology and Earth System Sciences*, 18(10), 4129-4151.
874 <https://doi.org/10.5194/hess-18-4129-2014>

1 **Ocean air masses dominate the land-surface atmospheric water cycles in**
2 **the coastal areas of Liaodong Bay: Insights from stable isotopes**

3
4 **Yi-Yuan Du^{1,2*}, Ri-Hong Wen^{3*}, Shristee Panthee¹, Sissou Zakari⁶, Liang Song¹,**
5 **Wen-Jie Liu¹, Bin Yang^{1†}**

6 ¹CAS Key laboratory of Tropical Forest Ecology, Xishuangbanna Tropical Botanical
7 Garden, Chinese Academy of Sciences, Menglun 666303, Yunnan, China.

8 ²University of Chinese Academy of Sciences, Beijing 100049, China.

9 ³Institute of Atmospheric Environment, China Meteorological Administration,
10 Shenyang, 110166, Liaoning, China.

11 ⁴Laboratory of Hydraulics and Environmental Modeling, Faculty of Agronomy,
12 Université de Parakou, Parakou, 03 BP 351, Benin.

13

14 Corresponding author: Yang Bin (yangbin@xtbg.ac.cn)

15 Menglun Yunnan, China; Tel.: 19969108917; Fax: 86-691-8715070

16 **Key Points:**

- 17 • Spatial-temporal variations of water vapor isotopes are very different during
18 2019/2020 growing (May-September) seasons.
- 19 • Meteorological variables are not reliable indicators for water vapor $\delta^2\text{H}$, $\delta^{18}\text{O}$,
20 and d-excess at Panjin experimental station.
- 21 • Ocean air masses from East Asian monsoon dominate land-surface
22 atmospheric water vapor cycles in the coastal areas of Liaodong Bay.

23

24 **Abstract**

25 Long-term atmospheric water vapor hydrogen ($\delta^2\text{H}$), oxygen ($\delta^{18}\text{O}$), and deuterium
26 excess (*d-excess*) can provide unique insights into the land-atmosphere coupling
27 processes. The in-situ measurements of atmospheric water vapor $\delta^2\text{H}$, $\delta^{18}\text{O}$, and *d-*
28 *excess* were conducted above a reed wetland of Liaodong Bay (2019-2020). We found
29 significant inter-annual variations in atmospheric water vapor isotopes between the
30 two growing (May-September) seasons. The $\delta^2\text{H}$, $\delta^{18}\text{O}$, and *d-excess* of atmospheric
31 water vapor exhibited different seasonal and diurnal cycles respect to the vertical (i.e.,
32 1 m, 3 m, and 5 m) measurement heights, especially in 2019. The isotopic differences
33 of atmospheric water vapor among vertical measurement heights were more evident
34 in the daytime (8:00-20:00 LST) than at night (20:00-8:00 LST). Rainfall events had a
35 direct impact on the diurnal patterns of water vapor isotopes, and the influences
36 depended on rainfall intensities. However, only weak correlations existed between
37 water vapor isotopes and local meteorological factors ($R^2 = 0.01-0.16$, $P < 0.001$),
38 such as water vapor concentration (w), relative humidity (RH), and surface air
39 temperature (T_a). Based on the back-air trajectory analyses, the spatial-temporal
40 dynamics of atmospheric water vapor isotopes highly synchronized with monsoon
41 activities. The dominant air masses in this region mainly arose from ocean sources,
42 which contributed to $62.1 \pm 12.2\%$ (49.4-84.5%) of the total air moisture. High *d-*
43 *excess* consistently followed the strong monsoon activities, suggesting predominating
44 impacts of ocean air masses from the East Asian monsoon region. High-resolution
45 measurements of atmospheric water vapor isotopes will improve our understanding of
46 the hydrological cycles in coastal areas.

47 **Plain Language Summary**

48 The coastal wetland regions in East Asia always have complex atmospheric
49 hydrological processes, because they are influenced both by the westerly belt and the
50 East Asian monsoon. Under such circumstances, still the question remains how do the
51 multiple air masses affect the seasonal and diurnal patterns of atmospheric
52 circulations? We implemented high temporal resolution (1Hz) measurements of
53 atmospheric hydrogen ($\text{HDO}/\text{H}_1\text{H}_2^{18}\text{O}$) and oxygen (H_2^{18}O and H_2^{16}O) using an off-
54 axis integrated cavity output spectroscopy (OA-ICOS) technology in a reed wetland.
55 The deuterium excess ($d\text{-excess} = \delta^2\text{H} - 8 \times \delta^{18}\text{O}$) of atmospheric water vapor was
56 further used as an indicator for identifying the moisture source locations (2019-2020).
57 There were obvious seasonal and diurnal variations of atmospheric water vapor $\delta^2\text{H}$,
58 $\delta^{18}\text{O}$, and *d-excess*. However, the inter-annual variations in atmospheric water vapor
59 isotopes were more notable in this study, mainly due to the stronger monsoon
60 activities. For example, the landing of typhoon “Lekima” brought a very high level of
61 atmospheric water vapor *d-excess* in 2019. Therefore, the local meteorological
62 variables might not be sufficient predictors of the atmospheric water vapor isotopes in
63 the coastal wetland regions.

64 **1 Introduction**

65 Measurements of atmospheric water vapor hydrogen ($\delta^2\text{H}$), oxygen ($\delta^{18}\text{O}$),
66 and deuterium excess (*d-excess*) can provide unique insights into the land-atmosphere
67 coupling processes (Gat, 1996; Lee et al., 2005; Vuille et al., 2003). The $\delta^2\text{H}$, $\delta^{18}\text{O}$,
68 and *d-excess* of water vapor (termed as the δ_{vapor} hereafter) can be used as natural
69 tracers of atmospheric water cycles (Bastrikov et al., 2014; Christner et al., 2017;
70 Munksgaard et al., 2020; Wen et al., 2008, 2010). Influenced by lower tropospheric
71 water variations (e.g., precipitation and vertical atmospheric mixing) and local
72 vegetation properties (e.g., soil evaporation and plant transpiration), the signatures of
73 land-surface water vapor δ_{vapor} contain subtle information concerning water
74 movements between the atmospheric boundary layer (ABL) and Earth's surfaces
75 (Huang & Wen, 2014; Laonamsai et al., 2021; Lee et al., 2006). Thus, there is a
76 growing interest in high-resolution measurements of atmospheric water vapor δ_{vapor}
77 from ecosystem to regional scales (Galewsky et al., 2016; Steen-Larsen et al., 2013;
78 Wei & Lee, 2019). Several studies have successfully completed the in-situ
79 atmospheric water vapor δ_{vapor} monitoring based on the technological advantages of
80 laser spectrometers (Aemisegger et al., 2014; Hu et al., 2014; Noone et al., 2012).
81 However, it is still necessary to conduct in-situ measurements of atmospheric water
82 vapor δ_{vapor} above near-surface ecosystems (Galewsky et al., 2016; Lee et al., 2005,
83 2007), compared with the condensed water isotopes that have formed a well-known
84 global network (e.g., Global Network of Isotopes in Precipitation, GNIP).

85 To the best of our knowledge, datasets of in-situ atmospheric water vapor
86 δ_{vapor} are reported across 49 sites worldwide. Those sites reflect the global land
87 surface in all forms, including oceans (e.g., Bonne et al., 2019; Galewsky et al., 2022;
88 Steen-Larsen et al., 2014a), forests (Aron et al., 2019; Bastrikov et al., 2014; Mercer
89 et al., 2020), grasslands (Hu et al., 2014; Parkes et al., 2017; Tremoy et al., 2014),
90 croplands (Griffis et al., 2016; Huang & Wen, 2014; Wen et al., 2012), ice sheets
91 (Bonne et al., 2020; Casado et al., 2016; Steen-Larsen et al., 2014b), cities (Christner
92 et al., 2017; Noone et al., 2012; Wang et al., 2021), and lakes (Cui et al., 2018; Hu et
93 al., 2021; Xiao et al., 2017). These studies confirm the great potential of in-situ water
94 vapor δ_{vapor} measurements to deconstruct the complex hydrological processes.
95 However, among the available data on atmospheric water vapor δ_{vapor} , the data from
96 coastal wetlands are scarce (Delattre et al., 2015; Lai et al., 2018). For example,
97 Delattre et al. (2015) showed that ground level atmospheric vapour composition can
98 record both local and regional isotopic signatures during 36 consecutive summer
99 days. The water vapor δ_{vapor} data reported by Lai et al. (2018) showed that, on daily
100 time scales (11-28 July, 2017), substantial rain recycling and large-scale atmospheric
101 water transport occur above a coastal mangrove forest in southern China, which is
102 subjected to the monsoons from South China Sea, Indian Ocean, Pacific Ocean, and
103 local land areas. Nevertheless, the brief campaigns of water vapor δ_{vapor} measurements
104 would restrain the best demonstration of atmospheric processes in the coastal
105 wetlands.

106 Previous studies have demonstrated that the small spatial and temporal variations of
107 atmospheric water vapor δ_{vapor} are affected mainly by processes of atmospheric
108 entrainments, land surface evapotranspiration (i.e., soil evaporation and plant
109 transpiration, ET), and vapor condensations (Huang & Wen, 2014; Lee et al., 2007;
110 Fiorella et al., 2019; Diekmann et al., 2021). Entrainment processes of the free
111 atmosphere will vertically deplete the ^2H and ^{18}O of water vapor near the land
112 surfaces (Devi et al., 2014; Kurita et al., 2012; Wei et al., 2015). Local ET will enrich
113 the ^2H and ^{18}O of near-surface atmosphere above the densely vegetated landscapes,
114 which usually plays a dominant role in the variations of water vapor δ_{vapor} (Lai &
115 Ehleringer, 2011; Zhang et al., 2011). The diurnal dynamics of atmospheric water
116 vapor δ_{vapor} are closely associated with the vapor condensation processes (e.g.,
117 precipitation, dew and fog), which is mainly caused by the equilibrium phase changes
118 of local water vapor during the synoptic events (Bailey et al., 2015; Farlin et al., 2013;
119 Wen et al., 2012). On large spatial scales, air mass advection is considered as a
120 critical factor contributing to the temporal variability in atmospheric water vapor δ_{vapor}
121 (Dahinden et al., 2021; Galewsky et al., 2011; Steen-Larsen et al., 2015).

122 Despite high-resolution monitoring efforts over the past two decades,
123 decoupling the atmospheric water vapor δ_{vapor} variability across various timescales
124 remains challenging (Bagheri et al., 2019; Berkelhammer et al., 2013; Lee et al.,
125 2005; Dahinden et al., 2021). The deuterium excess ($d\text{-excess} = \delta^2\text{H} - 8 \times \delta^{18}\text{O}$) of
126 atmospheric water vapor provides a new insight into the source identification of
127 atmospheric moistures (Dansgaard, 1964; Merlivat & Jouzel, 1979; Welp et al.,
128 2012). The theoretical basis of this application is that the $d\text{-excess}$ of water vapor is
129 closely linked to the environmental conditions during the kinetic fractionation
130 processes (Araguas-Araguas et al., 2000; Craig, 1961). Hence, the strong sensitivity
131 of $d\text{-excess}$ to local atmosphere relative humidity (RH) can place better constraints on
132 the water transport processes than the analyses of water vapor $\delta^2\text{H}$ and $\delta^{18}\text{O}$ alone
133 (Lai et al., 2018; Wei & Lee, 2019). Previous work has traced both the ocean moisture
134 sources (Dahinden et al., 2021; Gonzalez et al., 2016; Salamalikis et al., 2015) and
135 continental moisture recycling (Aemisegger et al., 2014; Fiorella et al., 2019). To
136 better resemble the transmission path of large-scale air masses, tools of Hybrid
137 Single-Particle Lagrangian Integrated Trajectory (HYSPPLIT) and TrajStat models
138 have been widely used in conjunction with water vapor isotopes in recent years
139 (Bagheri et al., 2019; Fiorella et al., 2018; Gonzalez et al., 2016; Salamalikis et al.,
140 2015). It is foreseeable that long-term water vapor $d\text{-excess}$ measurements will
141 improve our understanding of atmospheric processes and the associated mechanisms
142 in the coastal wetlands.

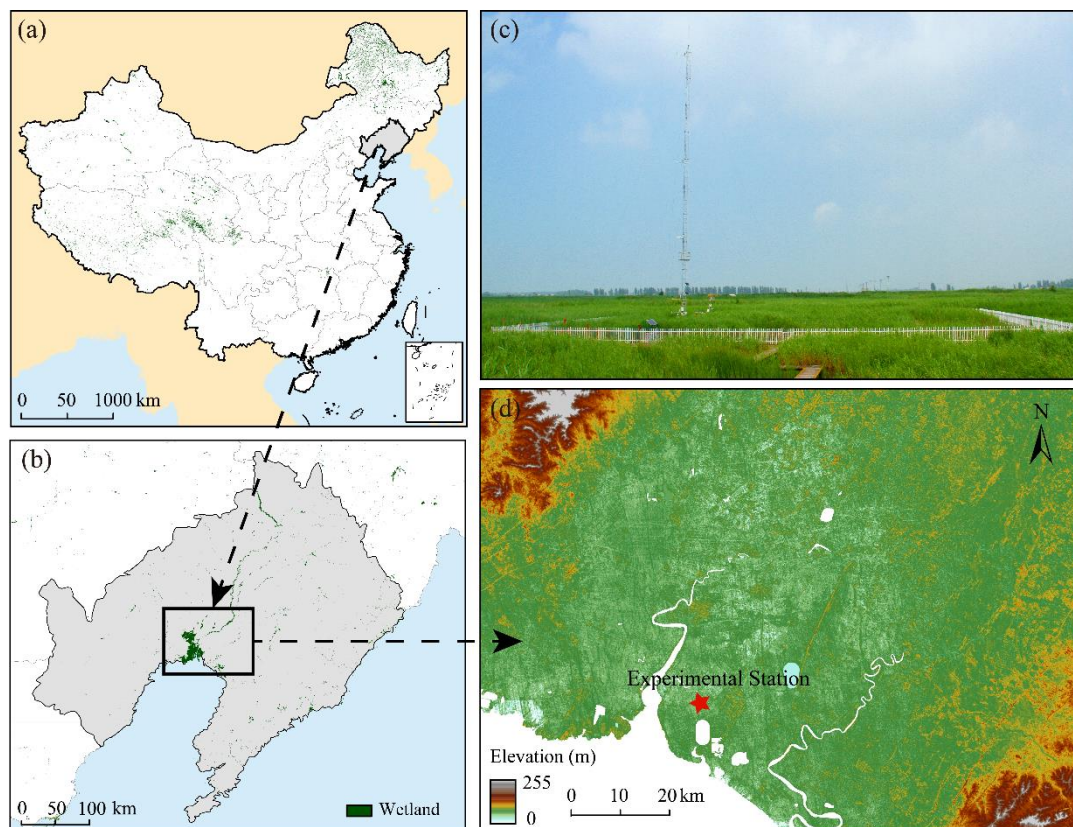
143 Liaodong Bay, a high-latitude continental bay (37.1-41.0° N, 117.6-121.2° E),
144 has the largest size and northernmost semi-enclosed seaports in China. It contains a
145 wetland area of approximately 5300 km² (Luo et al., 2021). According to the 2nd
146 National Wetland Survey Statistics Report (NFGA, 2010), the reed wetlands in this
147 region are well-preserved and among the largest in extent (~ 2500 km²) in the world.
148 Those offshore wetlands are located in the transition zones between continents and
149 oceans, which are vulnerable to natural and anthropogenic activities, such as urban

150 and agricultural runoff. To fill the gaps in knowledge regarding the mechanisms of
151 water cycle processes, we conducted two-year (2019-2020) measurements of
152 atmospheric water vapor $\delta^2\text{H}$, $\delta^{18}\text{O}$, and *d-excess* in the reed wetlands of Liaodong
153 Bay. The present study aims to (i) investigate the spatial-temporal dynamics of
154 atmospheric water vapor isotopes above the coastal wetland, and (ii) identify the
155 contributing factors that affect the isotopic characteristics of atmosphere in Liaodong
156 Bay. We hypothesize that (1) isotopic gradients exist for atmospheric water vapor
157 measurements along the monitoring heights due to the growth of reeds, and (2) moist
158 air masses from the East Asian monsoon strongly affects the atmospheric water vapor
159 isotopes.

160 **2 Materials and Methods**

161 2.1 Study site

162 The observations were carried out at Panjin Wetland Field Science
163 Experimental Station (40° 56' 40" N, 121° 56' 36" E, and elevation 2.1 m), located in
164 the north of Liaodong Bay. This station is a member of the National Climatic
165 Observatory of China Meteorological Administration (CMA), which is adjacent to the
166 Liaohe River Delta wetlands, and 12 km to the Bohai Sea (Figure 1a and 1b). This
167 area is characterized by the semi-humid temperate monsoon climate, influenced by
168 the westerly belt and the East Asian monsoon. The southwest East Asian monsoon
169 prevails from May to September, which brings abundant rainfall between July and
170 September (Huang et al., 2018). The regional meteorological records (1961-2010)
171 indicate that the mean air temperature and annual precipitation are 9.1 °C and 643.9
172 mm, respectively. Approximately 170 days of frost-free weather occur throughout the
173 year. The annual evaporation is about 516.0-720.3 mm (2012-2015). The research site
174 (150 m × 150 m) is situated in the center of a reed marsh (~ 780 km²), with a
175 vegetation coverage of more than 90% (Wang et al., 2016). Meteorological data of
176 surface air temperature (T_a), relative humidity (RH), and total precipitation (P)
177 obtained from an automatic weather station (Model A753WS, Adcon Telemetry Inc.,
178 Santa Rosa, CA). The leaf area index (LAI) and height of the reeds were collected for
179 fifteen days intervals during the growing season (May-September). During the study
180 periods of 2019 and 2020, the maximum LAI and maximum height were 5.1 m² m⁻²
181 and 2.5 m, respectively.



182

183 **Figure 1.** Maps showing the locations of Liaodong Bay (a, b) and Panjin
 184 experimental station (c, d) in this study. Elevation data was downloaded from the
 185 National Earth System Science Data Center, National Science & Technology
 186 Infrastructure of China (<http://www.geodata.cn>).

187

2.2 In-Situ measurement of water vapor isotopes

188

189

190

191

192

193

194

195

196

197

198

199

200

201

202

203

204

The in-situ system used to measure the atmospheric water vapor $\delta^2\text{H}$ and $\delta^{18}\text{O}$ consisted of a water vapor isotope analyzer (WVIA), a water vapor isotope standard source (WVISS), and an air sampling system (ASS). The WVIA was used to measure water vapor isotopes (at a frequency of 1 Hz) based on the off-axis integrated cavity output spectroscopy (OA-ICOS; Model TIWA-912, Los Gatos Research, Mountain View, CA, USA). The analyzer has a near-infrared diode laser scanning absorption lines ($\sim 1.4 \mu\text{b}$) for H_2^{16}O , H_2^{18}O , and $\text{H}_1\text{H}_2^{16}\text{O}$ (HDO), whose precision was approximately 0.4‰ for $\delta^2\text{H}$ and 0.08‰ for $\delta^{18}\text{O}$ (Steen-Larsen et al., 2013; Wen et al., 2012). The WVISS is an online calibration device that generates fixed concentrations of continuous vapor streams (Model 908-004-902, Los Gatos Research, Mountain View, CA, USA). In this study, ultrapure liquid water with known isotopic values was nebulized (at a rate of $2\text{-}10 \text{ L min}^{-1}$) to produce three designated gradients of standard streams (S_1 , S_2 , and S_3 , 300s each) covering the water vapor concentration of ambient air. There is no isotopic fractionation since the nebulizer and hot chamber (2 L) of WVISS will ensure instant evaporation (heated to $80 \text{ }^\circ\text{C}$) of all liquid water. The ASS was mounted on a 30 m height tower (Figure 1c) and used to pump ambient air from four heights (1, 3, 10, and 15 m) with 300s spent

205 on each height. To reduce the residence time of ambient air in the inlet lines (i.e.,
 206 “memory effects”), the sampling lines were pumped at approximately 2 L min⁻¹ using
 207 a commercial multiplexer (Model MC-2000-8, Lica United Technology Limited Inc.,
 208 Beijing, CHN). Teflon pipes were used in conjunction with individual heating tapes
 209 and jackets to prevent possible vapor condensation in the sampling tubes (Lee et al.,
 210 2005; Sturm & Knohl, 2010). Filters were installed at the entrances of the air-intake
 211 lines to prevent sucking liquid water into the instrument (Model 300-01961, LI-COR
 212 Inc., Lincoln, NE, USA). The switching sequence was S₁, S₂, S₃, and ambient air,
 213 with 15 minutes on the standard streams and 220 minutes on ambient air. The WVIA
 214 and WVISS were placed in an air-conditioning room to minimize the temperature-
 215 driven drifts.

216 While using the OA-ICOS for high-precision measurements of atmospheric
 217 water vapor $\delta^2\text{H}$ and $\delta^{18}\text{O}$, measurement bias can occur because of the instrumental
 218 concentration-dependence and time-drift (Bastrikov et al., 2014; Wen et al., 2008,
 219 2012). Here, we followed a user-configurable “two-point calibration” protocol
 220 described by Wen et al. (2012), Huang & Wen (2014) and Xiao et al. (2017). Every
 221 220 minutes (i.e., ~ 3.7 h) after the ambient (1, 3, 10, and 15 m) air measurements,
 222 two of the three standards (S₁, S₂, and S₃) spanning the water vapor concentration of
 223 ambient air were used to linearly calibrate atmospheric water vapor measurements.
 224 The isotopic values of the liquid calibration standards were measured using a liquid
 225 water isotope analyzer (Model GLA 431-TLWIA, Los Gatos Research, Mountain
 226 View, CA, USA), which were scaled to the Vienna Standard Mean Ocean Water
 227 (VSMOW) scale. For all the raw $\delta^2\text{H}$ and $\delta^{18}\text{O}$ measurements, the first 180 of 300 s
 228 spent measuring a given standard stream or an ambient vapor were discarded from the
 229 analysis to eliminate the possible memory effects. Then, the “two-point” linear
 230 interpolation was implemented using the following formula (Wen et al., 2012; Huang
 231 & Wen, 2014):

$$232 \quad \delta_{\text{vapor}} = \delta_{s1} + \frac{(\delta_{s2} - \delta_{s1})}{(X_{s2} - X_{s1})} \times (X_{\text{air}} - X_{s1}) \quad (1)$$

233 where δ_{vapor} is the isotopic ratio ($^2\text{H}/^1\text{H}$, or $^{18}\text{O}/^{16}\text{O}$) of one ambient air (i.e., 1,
 234 3, 10, and 15 m), δ_{s1} and δ_{s2} are the single-point corrected ambient airs that are
 235 normalized to a reference humidity (i.e., X_{s1} and X_{s2}), X_{s1} , X_{s2} and X_{s1} are water
 236 vapor concentrations of the two selected standard streams (S₁, S₂, and S₃) and the
 237 ambient air, respectively.

238 The isotopic data collected at 1 m, 3 m, and 15 m in height were used for
 239 representing the lower, middle, and upper canopy during the 2019-2020 growing
 240 (May-September) seasons. The second-order parameter deuterium excess ($d\text{-excess} =$
 241 $\delta^2\text{H} - 8 \times \delta^{18}\text{O}$) is defined as the deviation from the linear relationship between $^2\text{H}/^1\text{H}$
 242 and $^{18}\text{O}/^{16}\text{O}$ in the Global Meteoric Water Line (GMWL) having a mean slope of 8
 243 (Dansgaard, 1964; Merlivat & Jouzel, 1979). All data reported were block-averaged
 244 to hourly intervals.

245 2.3 Back-air mass trajectory analyses

246 The Hybrid Single Particle Lagrangian Integrated Trajectory (HYSPLIT)
 247 model was used to track changes in isotopic composition and moisture sources
 248 (Christner et al., 2018; Munksgaard et al., 2020). The HYSPLIT model
 249 (<https://ready.arl.noaa.gov/HYSPLIT.php>) was developed by the National Oceanic
 250 and Atmospheric Administration-Air Resources Laboratory (NOAA-ARL). Inputs of
 251 the HYSPLIT model include the cloud height, wind direction, temperature, and
 252 surface pressure, which are available from the Global Data Assimilation System
 253 (GDAS) meteorological data. In this study, the spatial resolution of the HYSPLIT
 254 model was set to $1^\circ \times 1^\circ$, and the starting height was set to 500 m above ground level.
 255 The 48-hour back-tracking analysis (close to the time that water vapor is present in
 256 the air) was performed hourly for the experimental site from May to September 2019
 257 and 2020. The angular distance of the TrajStat model
 258 (<http://www.meteothinker.com/downloads/index.html>) was used to cluster the
 259 trajectories of air mass reaching the experimental station:

$$260 \quad D = \frac{1}{n} \sum_{i=1}^n \left(0.5 \frac{A_i + B_i - C_i}{\sqrt{A_i B_i}} \right) \quad (2)$$

261 where D is the average angular distance between two backward trajectories, A
 262 and B are the squares of the straight-line distances between the trajectory points and
 263 the experimental site, and C denotes the square of the straight-line distance between
 264 the two trajectory points.

265 The Concentration Weighted Trajectory (CWT) method was used to identify
 266 the potential source regions contributing to the variability of atmospheric water vapor
 267 *d-excess* at the experimental site (Li et al., 2020; Salamalikis et al., 2015). The
 268 rearward trajectories were assigned by the equally sized $i \times j$ grid cells. The sample
 269 concentrations accompanying trajectories that traversed each grid cell were averaged
 270 to provide each grid cell with a weighted concentration. The calculation of this
 271 method could be found in Li et al. (2020):

$$272 \quad C_{ij} = \frac{1}{\sum_{l=1}^M \tau_{ijl}} \sum_{l=1}^M c_l \tau_{ijl} \quad (3)$$

273 where C_{ij} is the average *d-excess* concentration in the ij^{th} cell, l is the
 274 trajectory index, M is the total number of the trajectories, c_l is the concentration (*d-*
 275 *excess*) of the trajectory l , and τ_{ijl} is the time spent in the ij^{th} cell by the trajectory l .
 276 The weight function (W_{ij}) was further introduced ($WCWT_{ij} = C_{ij} \times W_{ij}$) to reduce
 277 uncertainty because the error of CWT increases with the distance between the grid
 278 and the experimental station.

279 2.4 Statistical analyses

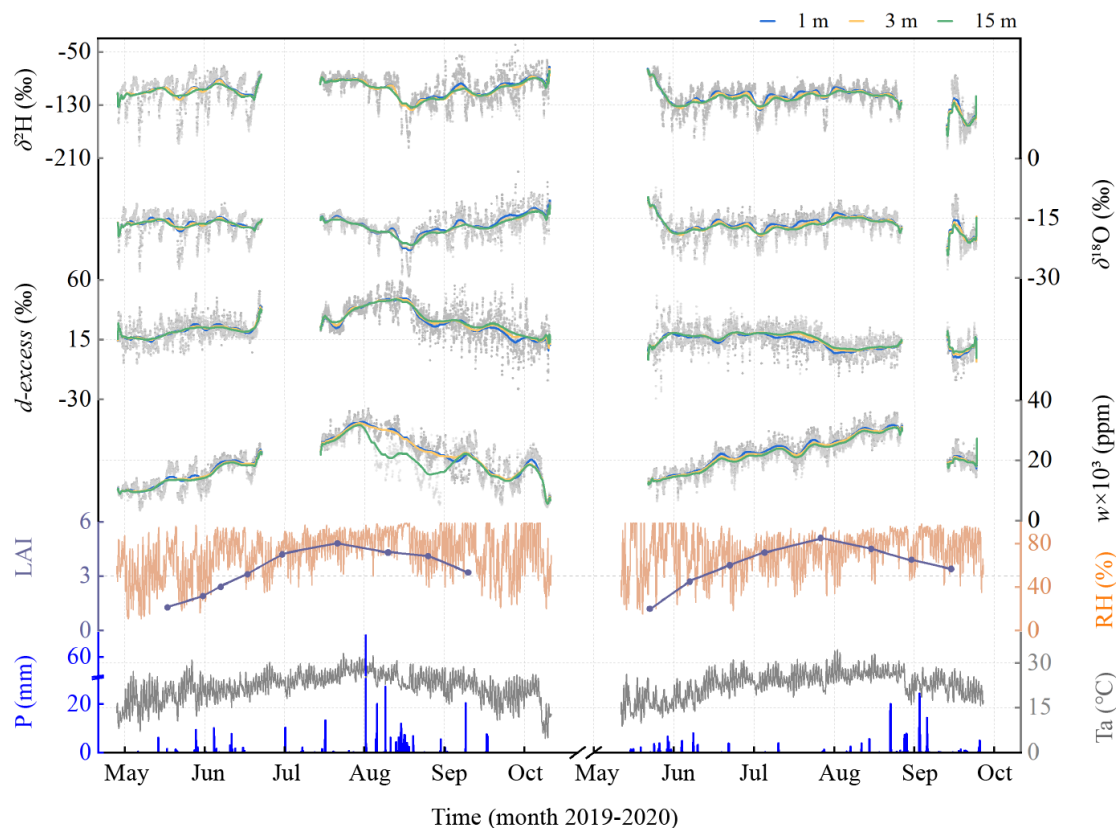
280 The isotopic data of atmospheric water vapor were calibrated based on the
281 “two-point calibration” protocol using Matrix Laboratory (MATLAB, version 9.2.0,
282 The MathWorks, Inc. Natick, USA). The normality and homogeneity of all data were
283 checked using IBM SPSS statistical software (Version 22.0, SPSS Inc., Chicago,
284 USA). One-way analysis of variance (ANOVA) and multiple means comparisons
285 (LSD) were used to highlight differences in data between months and vertical strata.
286 Considering the possible errors of the two variables, we used geometric mean
287 regression (GMR) to assess the relationships between atmospheric water vapor
288 isotopes and meteorological data with two probability levels of $P \leq 0.05$ and $P \leq$
289 0.001 .

290 **3 Results**

291 3.1 Long time scale variations

292 Figure 2 shows the seasonal variations in hourly measured atmospheric water
293 vapor $\delta^2\text{H}$, $\delta^{18}\text{O}$, and *d-excess* at lower (1 m), middle (3 m), and upper (15 m)
294 measurement heights during the 2019-2020 growing (May-September) seasons. The
295 meteorological data of water vapor concentration (*w*), leaf area index (LAI), relative
296 humidity (RH), total precipitation (P), and surface air temperature (T_a) are also
297 presented for the Panjin experimental station. The WVIA analyzer was under repairs
298 from June 20 to July 10, 2019, and from August 24 to September 9, 2020. For the rest
299 of the study periods, only short gaps occurred in the in-situ measurements of
300 atmospheric water vapor $\delta^2\text{H}$, $\delta^{18}\text{O}$, and *d-excess* due to the occasional system
301 downtimes (e.g., electricity interruption and/or analyzer breakdown). The monthly
302 average of the above isotopic values of atmospheric water vapor and meteorological
303 data are summarized in Table 1.

304 The $\delta^2\text{H}$, $\delta^{18}\text{O}$, and *d-excess* of atmospheric water vapor underwent
305 pronounced inter-annual and annual changes with months and vertical measurement
306 heights (Figure 2). Significant differences existed in atmospheric water vapor $\delta^2\text{H}$ (P
307 < 0.001), $\delta^{18}\text{O}$ ($P < 0.05$), and *d-excess* ($P < 0.001$) between 2019 and 2020. The
308 mean isotopic values of atmospheric water vapor were higher in 2019 ($\delta^2\text{H}$: $-108.4 \pm$
309 21.4% , $\delta^{18}\text{O}$: $-16.64 \pm 3.13\%$, and *d-excess*: $26.3 \pm 11.7\%$) than in 2020 ($-120.7 \pm$
310 20.2% , $-16.98 \pm 2.93\%$ and $13.3 \pm 8.4\%$). Variation amplitudes (i.e., maximums –
311 minimums) of the water vapor $\delta^2\text{H}$, $\delta^{18}\text{O}$, and *d-excess* were 153.8‰, 27.69‰, and
312 82.5‰ in 2019, and were 124.5‰, 20.78‰, and 77.7‰ in 2020. The $\delta^2\text{H}$ and $\delta^{18}\text{O}$ of
313 atmospheric water vapor gradually decreased with the vertical measurement heights
314 from 1 m to 3 m and 15 m in both 2019 and 2020. In contrast, the *d-excess* of water
315 vapor increased from the lower (1 m) to the upper (15 m) canopy during the two years
316 of study periods. The difference in atmospheric water vapor $\delta^2\text{H}$, $\delta^{18}\text{O}$, and *d-excess*
317 was only significant between 1 m and 15 m ($P < 0.05$) in 2019. The isotopic values of
318 atmospheric water vapor changed drastically between 1 m and 15 m ($P < 0.001$) in
319 2020; and the atmospheric water vapor $\delta^{18}\text{O}$ and *d-excess* differed significantly
320 between 1 m and 3 m ($P < 0.001$) in 2020.



321

322 **Figure 2.** Time series of hourly atmospheric water vapor $\delta^2\text{H}$, $\delta^{18}\text{O}$, and $d\text{-excess}$,
 323 water vapor concentration (w), leaf area index (LAI), relative humidity (RH),
 324 precipitation (P), and surface air temperature (T_a) during the 2019-2020 growing
 325 (May-September) seasons. The Gaussian smoothing curves are shown for the in-situ
 326 atmospheric water vapor measurements at heights of 1 m (blue lines), 3 m (yellow
 327 lines), and 15 m (green lines).

328 The w of atmospheric water vapor was highest in August with single-peaked
 329 curves of seasonal variations (Figure 2). However, the peak of water vapor w in 2019
 330 (36959.8 ppm) was delayed for 25 days compared to the peak (36090.8 ppm) in 2020.
 331 Furthermore, there were apparent differences in the atmospheric water vapor w
 332 between 1 m (or 3 m) and 15 m in 2019 ($P < 0.001$). During the growing (May-
 333 September) seasons, the LAI of reeds were 3.3 ± 1.2 in 2019 and 3.6 ± 1.2 in 2020.
 334 The mean RH in 2019 and 2020 were 70.7 ± 19.7 and 72.6 ± 17.5 , respectively. The
 335 total rainfall was 37.6% lower in 2020 (414.1 mm) compared to 2019 (663.8 mm),
 336 indicating a weak summer monsoon year in 2020. The T_a of the experimental station
 337 was relatively constant with mean values of 21.9 ± 4.7 °C in 2019 and 22.8 ± 4.3 °C
 338 in 2020 during the study periods.

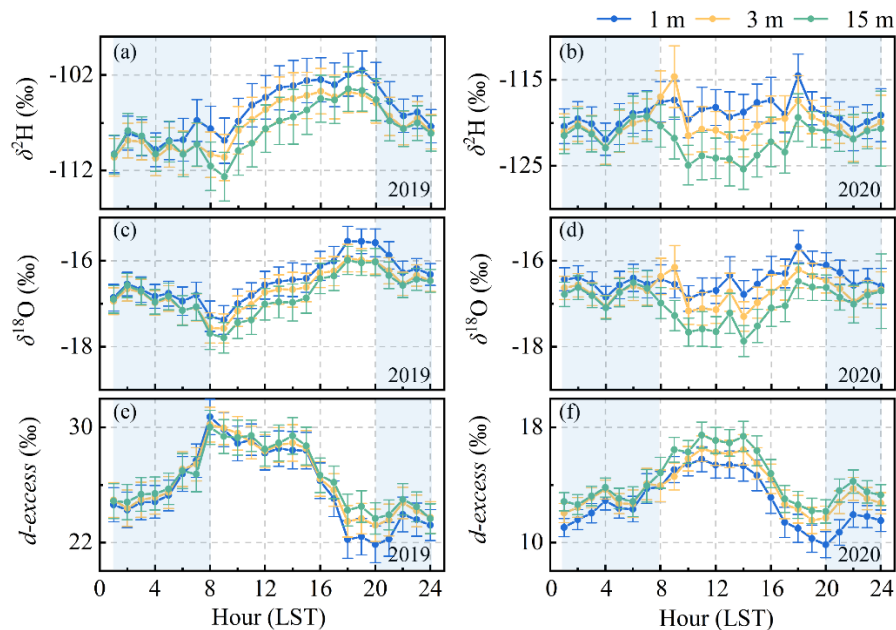
339 **Table 1** Monthly average values of Water Vapor Concentration (w), Leaf Area Index (LAI), Relative Humidity (RH), Total
 340 Precipitation (P), Surface Air Temperature (T_a), and Isotopic Values of Atmospheric Water Vapor ($\delta^2\text{H}$, $\delta^{18}\text{O}$, and $d\text{-excess}$) in
 341 Liaodong Bay, China, from May-September 2019 and 2020

Month	w (ppm) ^a	LAI (m ² m ⁻²)	RH (%)	P (mm)	T_a (°C)	$\delta^2\text{H}$ (‰)			$\delta^{18}\text{O}$ (‰)			$d\text{-excess}$ (‰)		
						1 m	3 m	15 m	1 m	3 m	15 m	1 m	3 m	15 m
May	12045.5	1.6	54.1	66.1	18.3	-111.1	-111.8	-112.5	-16.31	-16.40	-16.49	19.4	19.4	19.4
Jun	18875.6	3.3	69.4	44.9	22.0	-104.4	-105.8	-107.2	-16.10	-16.25	-16.31	24.4	24.2	23.3
Jul	29870.6	4.4	78.	55.8	25.6	-97.2	-97.5	-98.3	-12.79	-12.88	-13.00	33.7	34.1	34.2
Aug	25471.5	4.0	82.6	424.1	24.9	-113.2	-114.3	-115.0	-18.54	-18.77	-18.87	35.2	35.8	35.9
Sep	18040.9	3.2	70.1	107.9	26.0	-102.6	-104.9	-104.5	-15.47	-15.91	-16.02	21.2	22.2	23.4
May	14714.6	1.8	70.2	85.9	16.7	-117.9	-118.8	-119.2	-16.75	-16.93	-16.96	15.9	16.4	16.3
Jun	20746.6	3.4	64.6	29.2	23.1	-118.3	-120.3	-122.4	-16.99	-17.34	-17.61	17.6	18.4	18.6
Jul	25200.8	4.5	70.7	11.5	25.4	-113.1	-114.8	-116.3	-15.60	-16.03	-16.34	11.7	13.3	14.6
Aug	30488.3	4.2	80.6	253	25.5	-115.0	-115.7	-116.7	-15.46	-15.60	-15.76	8.6	9.0	9.4
Sep	20180.2	3.3	77.6	34.8	21.7	-144.3	-146.1	-148.7	-18.73	-19.09	-19.54	5.6	6.6	7.6

342 ^a The monthly w of atmospheric water vapor was calculated based on the average of data from the lower (1 m), middle (3 m), and
 343 upper (15 m) canopy.
 344

345 3.2 Long time scale variations

346 Figure 3 presents the diurnal variations of atmospheric water vapor $\delta^2\text{H}$, $\delta^{18}\text{O}$, and d -
 347 *excess* measured at heights of 1 m, 3 m, and 15 m. A clear diurnal cycle of water vapor $\delta^2\text{H}$,
 348 $\delta^{18}\text{O}$, and d -*excess* existed in both 2019 and 2020. The atmospheric water vapor $\delta^2\text{H}$ and $\delta^{18}\text{O}$
 349 generally increased from 9:00 (LST) to 18:00 (LST). Simultaneously, the $\delta^2\text{H}$ and $\delta^{18}\text{O}$ of water
 350 vapor progressively declined to their minimum around 8:00-9:00 (LST) on the next day (Figure
 351 3a-d). The diurnal variations of atmospheric water vapor $\delta^2\text{H}$ and $\delta^{18}\text{O}$ were less pronounced in
 352 2020 than in 2019. Nonetheless, the diurnal variations of atmospheric water vapor d -*excess* were
 353 pretty clear in both years of 2019 and 2020, which had an opposite diurnal trend to that of
 354 atmospheric water vapor $\delta^2\text{H}$ and $\delta^{18}\text{O}$ (Figure 3e-f). The isotopic differences of atmospheric
 355 water vapor across measurement heights (i.e., 1, 3, and 15 m) were more evident in the daytime
 356 (8:00-20:00 LST) than at night (20:00-8:00 LST). This phenomenon appeared extremely typical
 357 in 2020, during which the atmosphere water vapor $\delta^2\text{H}$ and $\delta^{18}\text{O}$ declined progressively with the
 358 increase of heights ($P < 0.05$).

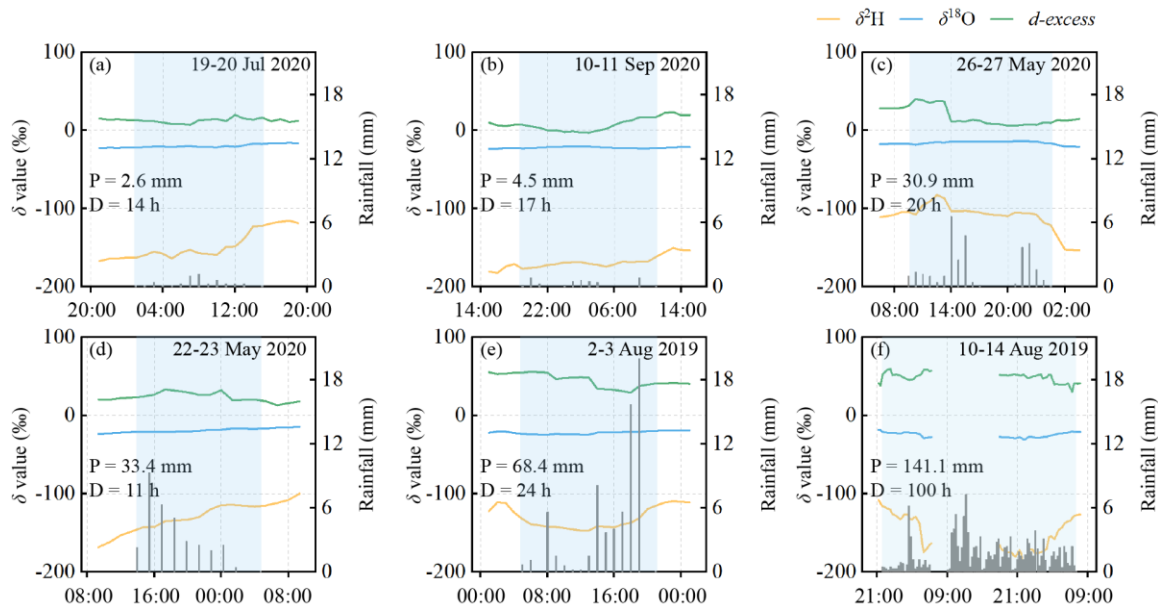


359

360 **Figure 3.** Twenty-four-hour variations of atmospheric water vapor $\delta^2\text{H}$ (a, b), $\delta^{18}\text{O}$ (c, d), and d -
 361 *excess* (e, f) measured at heights of 1 m (blue lines), 3 m (yellow lines), and 15 m (green lines)
 362 during the 2019-2020 growing (May-September) seasons. Error bars represent standard errors of
 363 the isotopic data in every hour. Shadow areas indicate the periods of time at night (20:00-8:00
 364 LST).

365 Figure 4 illustrates the impacts of rainfall processes on the diurnal cycles of atmospheric
 366 water vapor $\delta^2\text{H}$, $\delta^{18}\text{O}$, and d -*excess* at 15 m height. Six rainfall events of different rainfall
 367 amounts ($P = 2.6$ -141.1 mm) were selected during the 2019-2020 growing (May-September)
 368 seasons. The duration (D) of these rainfall events ranged from 11 h to 100 h. The $\delta^2\text{H}$, $\delta^{18}\text{O}$, and
 369 d -*excess* of atmospheric water vapor increased slightly after two small rainfall events ($P = 2.6$ -
 370 4.5 mm, in Figure 4a-b). The peak-to-peak variations of atmospheric water vapor $\delta^2\text{H}$, $\delta^{18}\text{O}$, and
 371 d -*excess* were 31.8-51.6‰, 3.08-7.02‰, and 12.7-26.2‰, respectively. With the increase in

372 intensity and duration of rainfall, the isotopic values of atmospheric water vapor also increased
 373 during the rainfall processes (Figure 4c-d). However, the isotopic values of atmospheric water
 374 vapor declined after a 20 h continuous rainfall event. The variability of atmospheric water vapor
 375 in these moderate rainfall events ($P = 30.9\text{-}33.4$ mm) increased to $68.4\text{-}70.8\text{‰}$ for $\delta^2\text{H}$, 7.15-
 376 8.87‰ for $\delta^{18}\text{O}$, and $20.3\text{-}34.3\text{‰}$ for $d\text{-}excess$. The $\delta^2\text{H}$, $\delta^{18}\text{O}$, and $d\text{-}excess$ of atmospheric water
 377 vapor decreased drastically during the heavy rainfall events as expected (Figure 4e-f). The
 378 isotopic variations of atmospheric water vapor in heavy rainfall events ($P = 68.4\text{-}141.1$ mm)
 379 were $37.4\text{-}66.8\text{‰}$ for $\delta^2\text{H}$, $3.41\text{-}5.70\text{‰}$ for $\delta^{18}\text{O}$, and $22.5\text{-}26.8\text{‰}$ for $d\text{-}excess$.



380

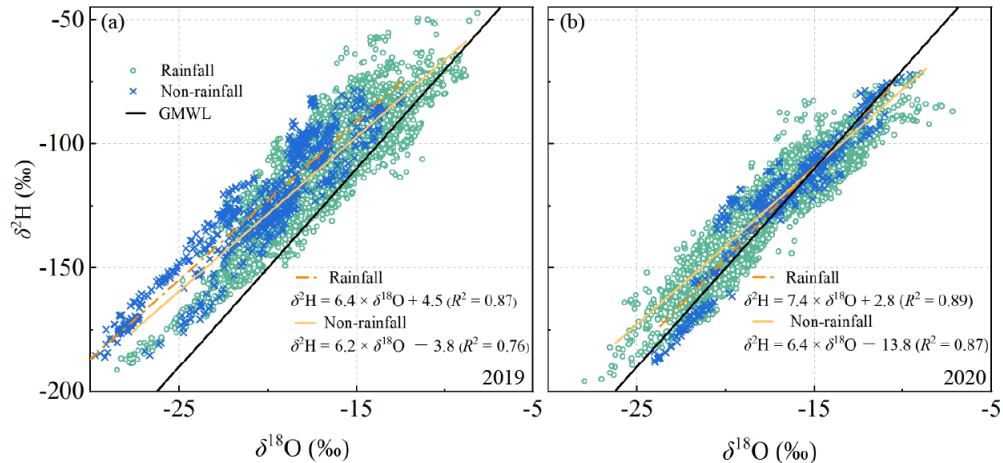
381 **Figure 4.** Impacts of rainfall processes on the diurnal cycles of atmospheric water vapor $\delta^2\text{H}$,
 382 $\delta^{18}\text{O}$, and $d\text{-}excess$ at 15 m height (a-f) during the (2019-2020) study periods. Rainfall amount
 383 (P) and rainfall duration (D) are plotted on each panel for reference. Shadow areas indicate the
 384 periods of rainfall events.

385

3.3 Relationships with meteorological variables

386

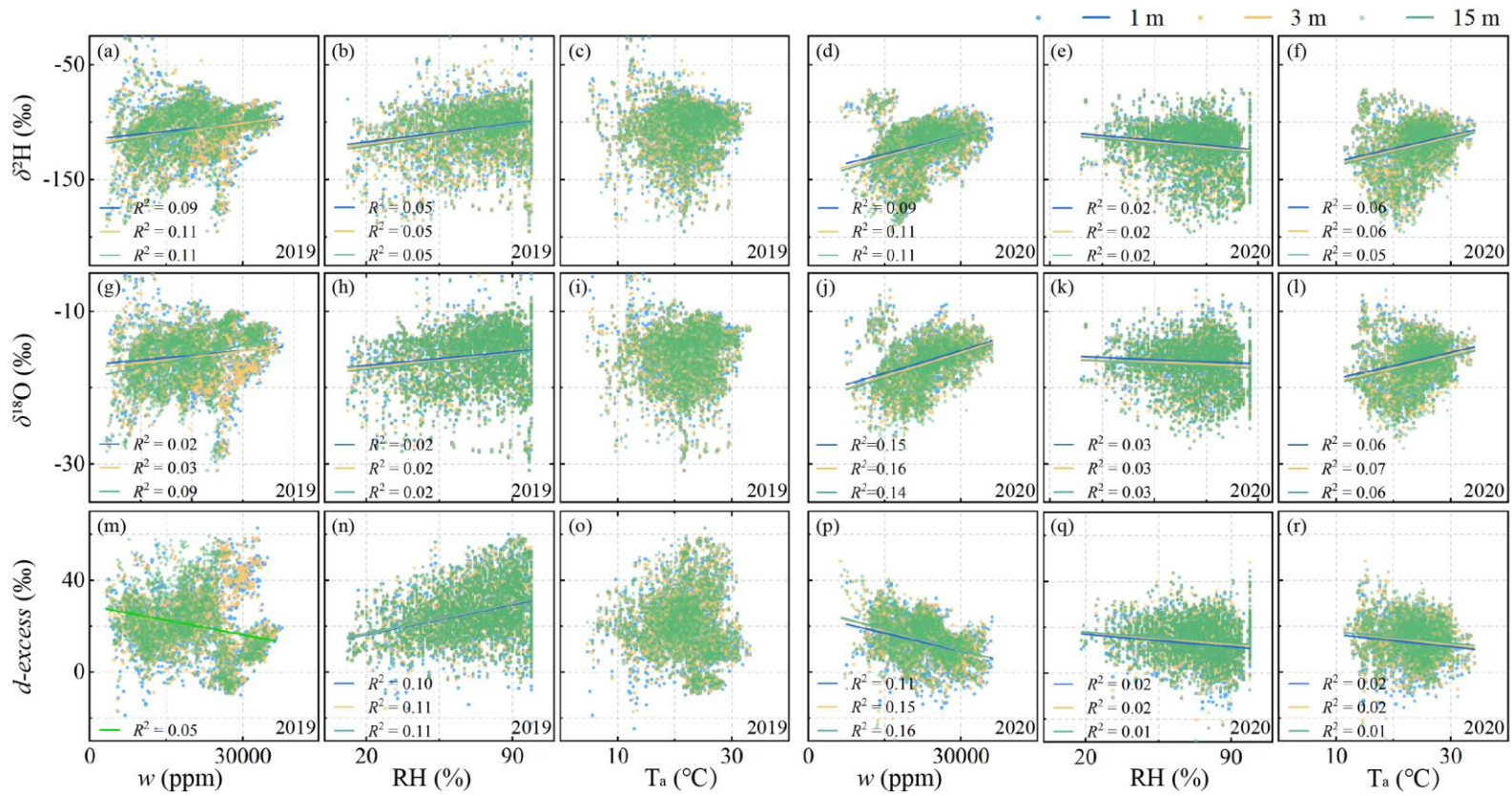
Figure 5 depicts the linear dependency of $\delta^2\text{H}$ on $\delta^{18}\text{O}$ for atmospheric water vapor
 387 during the 2019-2020 growing (May-September) seasons. The hourly measurement of three (i.e.,
 388 1 m, 3 m, and 15 m) canopy layers were merged to reflect the impacts of rainfall events on the
 389 co-variations between $\delta^2\text{H}$ on $\delta^{18}\text{O}$ of atmospheric water vapor. This treatment was adopted due
 390 to the similar functions among different heights (*SI Appendix A*, Figure S1). In 2019, the $\delta^2\text{H}$ and
 391 $\delta^{18}\text{O}$ of atmospheric water vapor mainly occupied the dual-isotope plots from the global meteoric
 392 water line (GMWL: $\delta^2\text{H} = 8 \times \delta^{18}\text{O} + 10$) to its left sides (Figure 5a). Slopes of the atmospheric
 393 water vapor lines in 2019 were 6.4 ± 0.2 ($R^2 = 0.87$, $P < 0.001$) and 6.2 ± 0.1 ($R^2 = 0.76$, $P <$
 394 0.001) during the rainfall and non-rainfall periods, respectively. In 2020, the $\delta^2\text{H}$ and $\delta^{18}\text{O}$ of
 395 atmospheric water vapor were plotted right on the GMWL (Figure 5b). Slopes of the
 396 atmospheric water vapor lines in 2020 were 7.4 ± 0.2 ($R^2 = 0.89$, $P < 0.001$) and 6.4 ± 0.1 ($R^2 =$
 397 0.87 , $P < 0.001$) during the rainfall and non-rainfall periods, respectively. The intercepts of the
 398 atmospheric water vapor lines were less than 10 for both years, ranging from 2.8 to 4.5 during
 399 the rainfall periods, and from -13.8 to -3.8 during the non-rainfall periods.



400

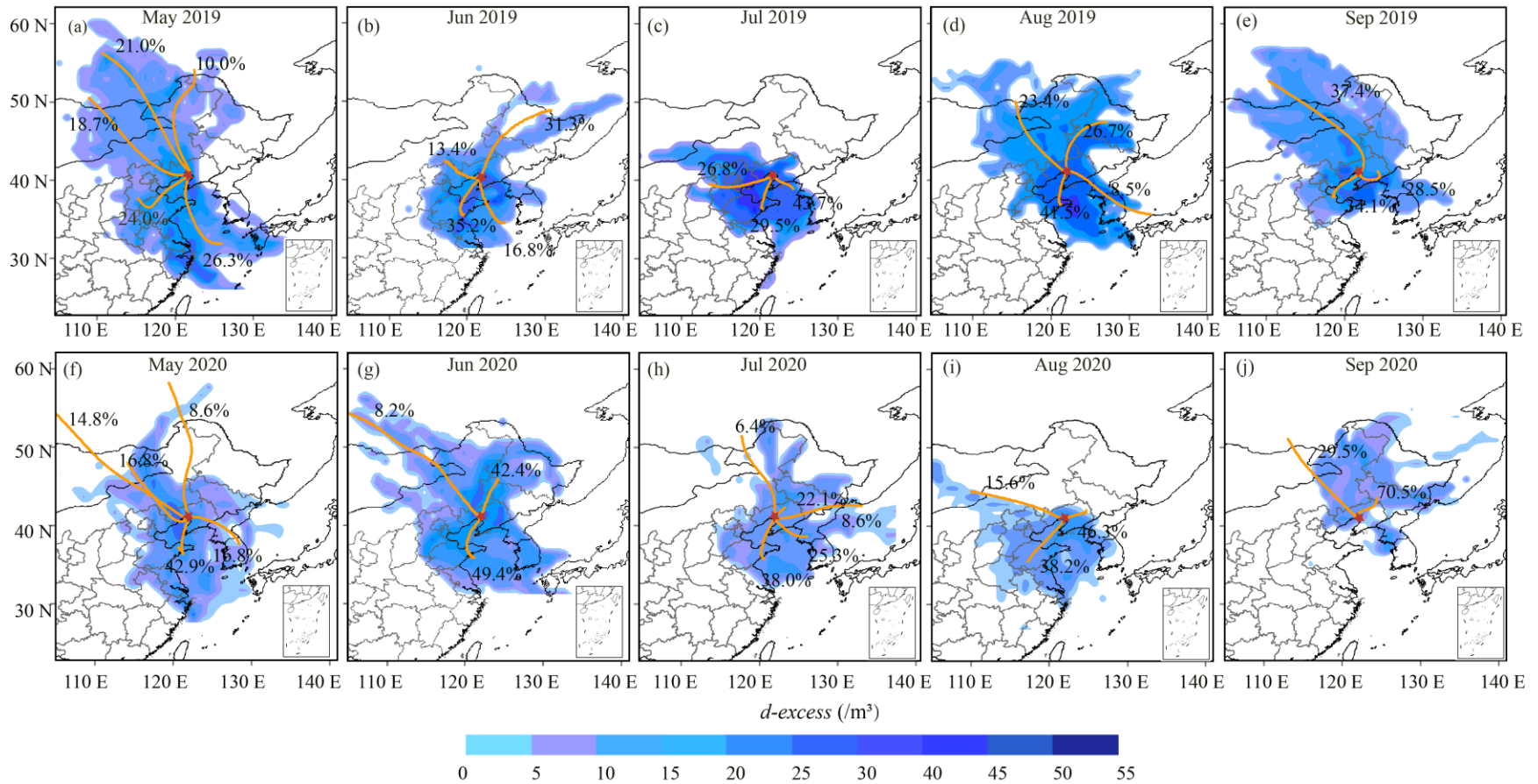
401 **Figure 5.** Isotopic values of $\delta^2\text{H}$ as a function of $\delta^{18}\text{O}$ in atmospheric water vapor during the
 402 2019 (a) and 2020 (b) growing (May-September) seasons. Data of atmospheric water vapor $\delta^2\text{H}$
 403 and $\delta^{18}\text{O}$ are divided into two groups representing the periods with rainfall and non-rainfall
 404 events. The global meteoric water line (GMWL: $\delta^2\text{H} = 8 \times \delta^{18}\text{O} + 10$) is also plotted on each
 405 panel for reference.

406 Figure 6 shows the relationships between the $\delta^2\text{H}$, $\delta^{18}\text{O}$ and d -excess of atmospheric
 407 water vapor and local meteorological factors. The $\delta^2\text{H}$ and $\delta^{18}\text{O}$ of atmospheric water vapor were
 408 positively correlated with the water vapor concentration (w) (Figure 6a, 6d, 6g, and 6j). In
 409 contrast, their d -excess were negatively correlated with w in 2019 ($R^2 = 0.05$, $P < 0.001$,
 410 measurement undertaken at height of 15 m, in Figure 6m) and 2020 ($R^2 = 0.11$ - 0.16 , $P < 0.001$,
 411 in Figure 6p). The atmospheric water vapor $\delta^2\text{H}$, $\delta^{18}\text{O}$ and d -excess were weakly dependent on
 412 the relative humidity (RH) during the study periods ($R^2 = 0.01$ - 0.11 , $P < 0.001$, in Figure 6b, 6e,
 413 6h, 6k, 6n, and 6q). The $\delta^2\text{H}$, $\delta^{18}\text{O}$ of atmospheric water vapor exhibited positive dependences on
 414 surface air temperature (T_a) in 2020 ($R^2 = 0.05$ - 0.07 , $P < 0.001$, in Figure 6f and 6l). The
 415 atmospheric water vapor d -excess in 2020 was negatively correlated with T_a ($R^2 = 0.01$ - 0.02 , $P <$
 416 0.001 , in Figure 6r). However, no significant correlation occurred between the atmospheric water
 417 vapor isotopes and T_a in 2019 (Figure 6c, 6i, and 6o).



418

419 **Figure 6.** Correlations of the water vapor concentration (w), relative humidity (RH), and surface air temperature (T_a) with the
 420 atmospheric water vapor $\delta^2\text{H}$ (a-f), $\delta^{18}\text{O}$ (g-l), and $d\text{-excess}$ (m-r) during the (2019-2020) study periods. The regression curves
 421 represent the in-situ atmospheric water vapor measurements at heights of 1 m (blue lines), 3 m (yellow lines), and 15 m (green lines).
 422



423
 424 **Figure 7.** Back trajectory frequencies clustered according to the directions of air masses and the concentration fields of atmospheric
 425 water vapor d -excess during the 2019 (a-e) and 2020 (f-j) growing (May-September) seasons. Red star indicates the location of Panjin
 426 experimental station. Orange lines are the clusters of air masses during the preceding 48 h at 500 m height above the ground, and blue
 427 shading is the potential source of atmospheric water vapor d -excess in each month.

428 3.4 Large scale atmosphere circulations

429 Figure 7 shows the concentration fields of atmospheric water vapor *d-excess* along the
430 backward trajectories at Panjin experimental station. The 48-hourly backward trajectories of air
431 masses were calculated for the 2019-2020 growing (May-September) seasons. For all five
432 months, 3659 and 3515 trajectories were clustered in 2019 and 2020, respectively (*SI Appendix*
433 *A*, Figure S2). Then, we identified three-five major moisture source sectors that affected the
434 experimental station. The dominant air masses in this region generally came from ocean sources,
435 contributing more than 50% to the total air moisture except in June 2020 (49.4%). The transport
436 paths of ocean air masses could be further clustered into two sectors, i.e., Southwest-South (SW-
437 S) and South-Southeast (S-SE) directions. At the beginning of the monsoon season (May-June),
438 the trajectory paths of air masses usually originated from ocean surfaces and the northern interior
439 (Figure 7a-b and 7f-g). The ocean air masses gradually dominated during the peak monsoon
440 season (July-August). The contribution proportions of ocean air masses reached the maxima in
441 July 2019 (73.2%, in Figure 7c) and in August 2020 (84.5%, in Figure 7i). The influence of
442 summer monsoon on local air masses weakened in September 2019, with a contribution
443 proportion of 59.9% (Figure 7e). However, the ocean air masses had a prolonged impact (70.5%)
444 on atmospheric water vapor *d-excess* at the experimental station in September 2020 (Figure 7j).

445 The back-air mass trajectory analysis indicates that seasonal dynamic in moisture sources
446 was a main driving factor of the atmospheric water vapor *d-excess* variability (Figure 7). The
447 spatial distribution of atmospheric water vapor *d-excess* at this experimental station was closely
448 linked with the monsoon activities in East Asia. Most of trajectory paths were accompanied by
449 relatively higher atmospheric water vapor *d-excess* in 2019 than in 2020. This phenomenon was
450 particularly evident in 2019 (Figure 7a-e), where high-value of atmospheric water vapor *d-excess*
451 commonly distributed around the coastal regions. Lower proportion of air masses arose from the
452 ocean sources between August and September in 2019 (50-59.9%, in Figure 7d-e) than in 2020
453 (70.5-84.5%, in Figure 7i-j). However, the intensity of the East Asian monsoon was weak in
454 2020, which brought less rainfall to the atmospheric water cycles in Liaodong Bay. Therefore,
455 the air masses from the interiors of North China had more significant impacts (i.e., more negative
456 values) on the atmospheric water vapor *d-excess* in 2020 than in 2019. The secondary moisture
457 sources of inland air masses played a vital role in the seasonal variations of atmospheric water
458 vapor *d-excess* in the weak summer monsoon year.

459

460 **4 Discussion**

461 Based on the in-situ measurement techniques, this study revealed the isotopic signatures of
462 atmospheric water vapor (Figure 2-4), as well as the driving forces of the atmospheric water
463 vapor isotopes (Figure 5-7) for a reed wetland of Liaodong Bay, Northeast China. The
464 meteorological factors (e.g., water vapor concentration, relative humidity, and air temperature)
465 were incapable of predicting the variations of atmospheric water vapor $\delta^2\text{H}$, $\delta^{18}\text{O}$, and *d-excess*
466 in this region. The different seasonal and diurnal patterns of water vapor isotopes could be
467 attributed to the stronger monsoon activities in 2019 than in 2020. These findings would broaden
468 our understanding of hydrological cycles in the coastal wetlands.

469

4.1 Temporal dynamics of water vapor isotopes at different heights

470

471 The long- (i.e., seasonal scale) and short- (i.e., diurnal scale) term characteristics of
472 atmospheric water vapor isotopes showed significant variations at heights of 1 m, 3 m, and 15 m
473 (Figure 2 and 3). The temporal dynamics of water vapor $\delta^2\text{H}$, $\delta^{18}\text{O}$, and *d-excess* are usually
474 controlled by the atmospheric processes (Lee et al., 2005; Wen et al., 2008), local
475 evapotranspiration (Aron et al., 2019; Huang & Wen, 2014), and synoptic events (Berkelhammer
476 et al., 2013; Wu et al., 2019). For instance, Steen-Larsen et al. (2013) suggested that the intra-
477 seasonal variations of water vapor isotopes mainly result from the interplay between large-scale
478 moisture advection, boundary layer dynamics, and local moisture fluxes above the Greenland Ice
479 Sheet. The magnitude of changes in surface water vapor *d-excess* can be as high as 40‰ or
480 greater during several episodes (Steen-Larsen et al., 2013). Huang & Wen (2014) reported that
481 the atmospheric water vapor $\delta^2\text{H}$, $\delta^{18}\text{O}$, and *d-excess* are dominated by the typical arid and
482 continental climates, which will not show clear seasonal cycles in the inland region of Northwest
483 China. As a typical coastal wetland under the influence of the East Asian Monsoon, our results
484 showed that the temporal patterns of water vapor isotopes were strikingly different between the
485 years of study periods. Moreover, some departures of atmospheric water vapor isotopes were
486 observed among the three measurement heights. This might be interpreted as the enrichment
487 effects of local evapotranspiration, which gradually improves the atmospheric water vapor
isotopes with the increasing plant physiological activities (Hu et al., 2021; Welp et al., 2012).

488

The seasonal variations of atmospheric water vapor $\delta^2\text{H}$, $\delta^{18}\text{O}$, and *d-excess* in the reed
489 wetlands of Liaodong Bay were different from those of the other research site (Fiorella et al.,
490 2018; Laonamsai et al., 2021; Lee et al., 2006; Wen et al., 2010). Apart from the noticeable
491 seasonal changes occurring in each year, there were distinct inter-annual cycles for atmospheric
492 water vapor isotopes between 2019 and 2020 (Figure 2). The mean isotopic values of
493 atmospheric water vapor ranged from -120.7‰ to -108.4‰ for $\delta^2\text{H}$, from -16.98‰ to $-$
494 16.64‰ for $\delta^{18}\text{O}$, and from 13.3‰ to 26.3‰ (Table 1), which were higher than the results
495 reported by Wen et al. (2010) and Zhang et al. (2011) in inland areas of China. Especially in
496 2019, the $\delta^2\text{H}$ and $\delta^{18}\text{O}$ of atmospheric water vapor fluctuated seasonally with lower values in
497 the prevailing monsoon season (i.e., August-September). The seasonal pattern of atmospheric
498 water vapor $\delta^2\text{H}$ and $\delta^{18}\text{O}$ made a complete reversal of the water vapor concentration (*w*) trend
499 (Figure 2). In fact, the summer monsoon was earlier in 2019 and brought more rainfall than in
500 2020. In 2019, the typhoon “Lekima” was reported to land in Southwest coast of China (4-10
501 August) with a wind speed of 51.4 m s^{-1} , which then moved northwards and made a second
502 landfall in Liaodong Bay (Wang et al., 2021). Some studies reported that a significant decrease
503 in precipitation and atmospheric isotopes can happen during the tropical typhoons (Bonne et al.,
504 2019; Conroy et al., 2016). The abrupt decline of atmospheric water vapor *w* at 15 m height
505 could also be attributed to the high condensation efficiency and strong entrainment activity
506 during the typhoon event in 2019.

507

The interactions between atmospheric entrainment and local evapotranspiration typically
508 dominate the diurnal cycles of atmospheric water vapor $\delta^2\text{H}$, $\delta^{18}\text{O}$, and *d-excess* (Aron et al.,
509 2019; Huang & Wen, 2014; Lee et al., 2007; Zhao et al., 2014). Our results showed that the $\delta^2\text{H}$
510 and $\delta^{18}\text{O}$ of atmosphere were lower in the early morning (8:00-9:00 LST) than in the late
511 afternoon (16:00-18:00 LST). On the contrary, the atmospheric water vapor *d-excess* exhibited
512 an “inverted U-shaped diurnal pattern” in 2019 and 2020 (Figure 3). The downward trends in
513 atmospheric water vapor $\delta^2\text{H}$ and $\delta^{18}\text{O}$ can be attributed to the rapid increase of free air in ABL

514 when plant transpiration activity is relatively low in the morning (Huang & Wen, 2014). The
515 enrichment roles of local evapotranspiration surpassed the depletion effects of atmospheric
516 entrainment in the late afternoon. Such positive impacts of local evapotranspiration on
517 atmosphere isotopes were marked significantly in the lower (1 m) canopy than in the middle (3
518 m) and upper (15 m) heights (Figure 3). Apparently, the rainfall process was one of the main
519 factors contributing to the diurnal dynamics of atmospheric water vapor $\delta^2\text{H}$, $\delta^{18}\text{O}$, and *d-excess*
520 (Figure 4). The isotopic fractionation caused by the sub-cloud secondary evaporation enriches
521 the residual rainfall, which in turn can make the enrichment of atmospheric isotopes during small
522 rainfall events (Vuille et al., 2003; Wu et al., 2021). However, the rainout effects of rainfall
523 would result in the continuous depletion of atmospheric isotopes according to the Rayleigh
524 distillation mechanisms (Gat, 1996; Lee et al., 2005; Wen et al., 2010).

525 4.2 Controlling factors of water vapor isotopes above coastal wetlands

526 The global meteoric water line (GMWL: $\delta^2\text{H} = 8 \times \delta^{18}\text{O} + 10$) indicates the isotopic co-
527 variations in marine water that has not been exposed to evaporation fractionation (Craig, 1961;
528 Gat, 1996). As the marine air masses move over the coastal regions and towards the inland, the
529 air parcels will be mixed with continental water vapor sources and influenced by geographic
530 parameters such as the distances from coasts, altitudes, rainfall processes, and temperatures
531 (Christner et al., 2018; Gat, 1996; Merlivat & Jouzel, 1979). The slopes of atmospheric water
532 vapor lines (6.2-7.4) were lower than that of GMWL (Figure 5), which were determined by the
533 non-equilibrium fractionation (i.e., the existence of kinetic effects) within air parcels. Similarly,
534 Bastrikov et al. (2014) reported that the overall slopes of atmospheric water vapor lines are 5.6-
535 7.7 among different seasons in western Siberia (Kourovka). Li et al. (2020) highlighted that the
536 slopes of atmospheric water vapor lines change from 7.0 to 7.6 during a six-year period in
537 Eastern China. The high intercept (i.e., *d-excess*) of atmospheric water vapor lines in 2019
538 suggested that the isotopic changes in air masses which were very sensitive to the moisture
539 source conditions (Aemisegger et al., 2014; Delattre et al., 2015; Fiorella et al., 2018).

540 The results of this study also showed that the relationships between local meteorological
541 factors and atmospheric water vapor isotopes were weak or nonexistent at Panjin experimental
542 station (Figure 6). This finding was inconsistent with previous observations in the inland areas of
543 China. For example, Zhang et al. (2011) noted that the water vapor concentration (*w*) can be an
544 excellent predictor of atmospheric water vapor $\delta^2\text{H}$, $\delta^{18}\text{O}$, and *d-excess* based on the Rayleigh
545 distillation. However, the weak correlations between atmospheric water vapor isotopes and
546 relative humidity (RH) were found in other studies (Li et al., 2020; Salamalikis et al., 2015). An
547 earlier study by Lee et al. (2006) in New England found that the atmospheric *w* is a better
548 indicator for atmospheric water vapor isotopes than air temperature (T_a) on short time scales.
549 These studies have established a certain level of correlation between atmospheric water vapor
550 isotopes and local meteorological factors (e.g., *w*, T_a , and RH) during the non-monsoon season
551 (Lee et al., 2005; Li et al., 2020; Noone et al., 2012). In contrast, Wen et al. (2010) found that the
552 *w* becomes a poor predictor of the atmospheric water vapor $\delta^2\text{H}$, $\delta^{18}\text{O}$, and *d-excess* during the
553 summer monsoon season. Similar to this study, weak correlations were also found by Li et al.
554 (2020) and Wang et al. (2021) during the peak monsoon activities.

555 Unlike the $\delta^2\text{H}$ and $\delta^{18}\text{O}$ whose temporal variations are commonly overwhelmed by the
556 Rayleigh distillation and/or the rainout history of air masses, the atmospheric water vapor *d-*
557 *excess* of an air mass is a nearly constant tracer during the transport processes (Welp et al., 2012;

558 Wei et al., 2019). Therefore, the *d-excess* of atmospheric water vapor is widely used as a
559 conservative indicator for identifying the moisture source locations (Aemisegger et al., 2014;
560 Steen-Larsen et al., 2015; Uemura et al., 2008; Xu et al., 2022). Panjin experimental station was
561 situated on the special borderland between the North China Plain and Bohai Sea (Figure 1),
562 which was also located within the edge of the East Asian monsoon region (Luo et al., 2021;
563 Wang et al., 2021). With the sea in three directions, the atmospheric water vapor *d-excess* in this
564 study was significantly affected by the ocean air masses (Figure 7). The high values of
565 atmospheric water vapor *d-excess* consistently appeared in the peak (i.e., July-August) monsoon
566 season. The results of the present study further confirmed that the ocean air masses dominated
567 the temporal variations of atmospheric water vapor *d-excess* (Figures 2, 3, and 7) when a super
568 typhoon “Lekima” happened in 2019 (details in Section 4.1). Lai et al. (2018) examined the
569 atmospheric water cycling above a coastal mangrove forest in Southern China. They also found
570 that the substantial increase of atmospheric water vapor *d-excess* is related to the passage of a
571 tropical typhoon “Talas” (Lai et al., 2018). In the Qinghai-Tibetan Plateau of central Asia, Wu et
572 al. (2019) revealed that high *d-excess* values of atmospheric water vapor were influenced by
573 local moisture mixing during the monsoon season. A recent study noted that high values of
574 atmospheric water vapor *d-excess* appear before the monsoon onset and after the monsoon
575 season at Lhasa in Southern Tibetan Plateau (Tian et al., 2020). Indeed, air masses from cold and
576 dry areas can also bring a relatively high atmospheric water vapor *d-excess* (Uemura et al., 2008;
577 Xu et al., 2022). Further mechanism studies are expected to provide more rational explanations
578 for the above-mentioned processes in coastal wetlands.

579

580 **5 Conclusions**

581 The inter-annual variations of atmospheric water vapor $\delta^2\text{H}$, $\delta^{18}\text{O}$, and *d-excess* were
582 significantly different between 2019 and 2020. On a seasonal time scale, the mean isotopic
583 values of atmospheric water vapor in 2019 were significantly higher than that in 2020.
584 Meanwhile, the $\delta^2\text{H}$ and $\delta^{18}\text{O}$ of atmospheric water vapor gradually decreased from the lower (1
585 m), to the middle (3 m) and upper (15 m) canopy both 2019 and 2020. A clear diurnal cycle of
586 atmospheric water vapor isotopes existed during the study periods, which was more pronounced
587 in 2019 than in 2020. The diurnal isotopic differences of atmospheric water vapor among
588 measurement heights (i.e., 1, 3, and 15 m) were more evident in the daytime (8:00-20:00 LST)
589 than at night (20:00-8:00 LST). Rainfall events had a significant impact on the diurnal dynamics
590 of atmospheric water vapor $\delta^2\text{H}$, $\delta^{18}\text{O}$, and *d-excess*, depending on the rainfall intensity (i.e.,
591 amount and duration). The correlations between atmospheric water vapor isotopes and local
592 meteorological factors were weak or nonexistent in the study region. Instead, the spatial-
593 temporal dynamics of atmospheric water vapor isotopes were highly consistent with the
594 monsoon activities. The moisture in air masses could be clustered into three to-five primary
595 sources, with over 60% from the ocean sources. High *d-excess* values reflected the
596 predominating influences of ocean air masses on atmospheric water vapor cycles in the coastal
597 regions.

598

599 **Acknowledgments**

600 We are deeply thankful to Ye Zhang, Long Chen, Xian-zhe Liu, and Han Wang (Panjin National
601 Climatic Observatory, Institute of Atmospheric Environment, China Meteorological
602 Administration) for field support. We would like to extend our thanks to Institutional Center for
603 Shared Technologies and Facilities of Xishuangbanna Tropical Botanical Garden, Chinese
604 Academy of Sciences for laboratory process support. We also acknowledge the NOAA-Air
605 Resources Laboratory (ARL) for providing the HYSPLIT model and meteorological data. This
606 research was supported by the National Natural Science Foundation of China [32171557,
607 32171529], the Yunnan Natural Science Foundation [202201AT070221], the Youth Innovation
608 Promotion Association of Chinese Academy of Sciences [2021397], the National Science and
609 Technology Basic Resources Survey Program of China [2019FY0101302], the National Key
610 R&D Program of China [2022YFF0801301], the Key Project of Liaoning Provincial
611 Meteorological Bureau [LNCP202205].

612

613 **Open Research**

614 Data for this study consist of water isotopes and environmental variables that are available at
615 <https://doi.org/10.11888/Atmos.tpd.272899>

616

617 **References**

- 618 Aemisegger, F., Pfahl, S., Sodemann, H., Lehner, I., Seneviratne, S. I., & Wernli, H. (2014).
619 Deuterium excess as a proxy for continental moisture recycling and plant transpiration.
620 *Atmospheric Chemistry and Physics*, 14(8), 4029-4054. [https://doi.org/10.5194/acp-14-](https://doi.org/10.5194/acp-14-4029-2014)
621 [4029-2014](https://doi.org/10.5194/acp-14-4029-2014)
- 622 Araguas-Araguas, L., Froehlich, K., Rozanski, K. (2000). Deuterium and oxygen-18 isotope
623 composition of precipitation and atmospheric moisture. *Hydrological Processes*, 14(8),
624 1341-1355. [https://doi.org/10.1002/1099-1085\(20000615\)14:8<1341::Aid-](https://doi.org/10.1002/1099-1085(20000615)14:8<1341::Aid-hyp983>3.0.Co;2-z)
625 [hyp983>3.0.Co;2-z](https://doi.org/10.1002/1099-1085(20000615)14:8<1341::Aid-hyp983>3.0.Co;2-z)
- 626 Aron, P. G., Poulsen, C.J., Fiorella, R. P., & Matheny, A. M. (2019). Stable water isotopes reveal
627 effects of intermediate disturbance and canopy structure on forest water cycling. *Journal of*
628 *Geophysical Research: Biogeosciences*, 124(10), 2958-2975.
629 <https://doi.org/10.1029/2019jg005118>
- 630 Bagheri, R., Bagheri, F., Karami, G. H., & Jafari, H. (2019). Chemo-isotopes (^{18}O & ^2H)
631 signatures and HYSPLIT model application: Clues to the atmospheric moisture and air mass
632 origins. *Atmospheric Environment*, 215, 116892.
633 <https://doi.org/10.1016/j.atmosenv.2019.116892>
- 634 Bailey, A., Noone, D., Berkelhammer, M., Steen-Larsen, H. C., & Sato, P. (2015). The stability
635 and calibration of water vapor isotope ratio measurements during long-term deployments.
636 *Atmospheric Measurement Techniques*, 4521-4538. [https://doi.org/10.5194/amt-8-4521-](https://doi.org/10.5194/amt-8-4521-2015)
637 [2015](https://doi.org/10.5194/amt-8-4521-2015)
- 638 Bastrikov, V., Steen-Larsen, H. C., Masson-Delmotte, V., Griбанov, K., Cattani, O., Jouzel, J., &
639 Zakharov, V. (2014). Continuous measurements of atmospheric water vapour isotopes in

- 640 western Siberia (Kourovka). *Atmospheric Measurement Techniques*, 7(6), 1763-1776.
641 <https://doi.org/10.5194/amt-7-1763-2014>
- 642 Berkelhammer, M., Hu, J., Bailey, A., Noone, D. C., Still, C. J., Barnard, H., et al. (2013). The
643 nocturnal water cycle in an open-canopy forest. *Journal of Geophysical Research:*
644 *Atmospheres*, 118(17), 10225-10242. <https://doi.org/10.1002/jgrd.50701>
- 645 Bonne, J. L., Behrens, M., Meyer, H., Kipfstuhl, S., Rabe, B., Schönicke, L., et al. (2019).
646 Resolving the controls of water vapour isotopes in the Atlantic sector. *Nature*
647 *Communications*, 10(1), 1-10. <https://doi.org/10.1038/s41467-019-09242-6>
- 648 Bonne, J. L., Meyer, H., Behrens, M., Boike, J., Kipfstuhl, S., Rabe, B. et al. (2020). Moisture
649 origin as a driver of temporal variabilities of the water vapour isotopic composition in the
650 Lena River Delta, Siberia. *Atmospheric Chemistry and Physics*, 20(17), 10493-10511.
651 <https://doi.org/10.5194/acp-20-10493-2020>
- 652 Casado, M., Cauquoin, A., Masson-Delmotte, V., Genthon, C., Kerstel, E., Kassi, S., et al.
653 (2016). Continuous measurements of isotopic composition of water vapour on the East
654 Antarctic Plateau. *Atmospheric Chemistry and Physics*, 16(13), 8521-8538.
655 <https://doi.org/10.5194/acp-16-8521-2016>
- 656 Christner, E., Aemisegger, F., Pfahl, S., Werner, M., Cauquoin, A., Schneider, M. et al. (2018).
657 The climatological impacts of continental surface evaporation, rainout, and subcloud
658 processes on δD of water vapor and precipitation in Europe. *Journal of Geophysical*
659 *Research: Atmospheres*, 123(8), 4390-4409. <https://doi.org/10.1002/2017jd027260>
- 660 Christner, E., Kohler, M., & Schneider, M. (2017). The influence of snow sublimation and
661 meltwater evaporation on δD of water vapor in the atmospheric boundary layer of central

- 662 Europe. *Atmospheric Chemistry and Physics*, 17(2), 1207-1225.
663 <https://doi.org/10.5194/acp-17-1207-2017>
- 664 Conroy, J. L., Noone, D., Cobb, M. K., Moerman, J. W., & Konecky, B. L. (2016). Paired stable
665 isotopologues in precipitation and vapor: A case study of the amount effect within western
666 tropical Pacific storms. *Journal of Geophysical Research: Atmospheres*, 121(7), 3290-3303.
667 <https://doi.org/10.1002/2015jd023844>
- 668 Craig, H. (1961). Isotopic variations in meteoric waters. *Science*, 133(346), 1702-1703.
669 <https://doi.org/10.1126/science.133.3465.1702>
- 670 Cui, J. P., Tian, L. D., & Gibson, J. J. (2018). When to conduct an isotopic survey for lake water
671 balance evaluation in highly seasonal climates. *Hydrological Processes*, 32(3), 379-387.
672 <https://doi.org/10.1002/hyp.11420>
- 673 Dahinden, F., Aemisegger, F., Wernli, H., Schneider, M., Diekmann, C.J., Ertl, B., et al. (2021).
674 Disentangling different moisture transport pathways over the eastern subtropical North
675 Atlantic using multi-platform isotope observations and high-resolution numerical
676 modelling. *Atmospheric Chemistry and Physics*, 21(21), 16319-16347.
677 <https://doi.org/10.5194/acp-21-16319-2021>
- 678 Dansgaard W. (1964). Stable isotopes in precipitation. *Tellus*, 16(4): 436-468.
679 <https://doi.org/10.3402/tellusa.v16i4.8993>
- 680 Delattre, H., Vallet-Coulomb C., & Sonzogni, C. (2015). Deuterium excess in the atmospheric
681 water vapour of a Mediterranean coastal wetland: regional vs. local signatures. *Atmospheric
682 Chemistry and Physics*, 15(17), 10167-10181. <https://doi.org/10.5194/acp-15-10167-2015>

- 683 Devi, P., Jain, A. K., Rao, M. S., & Kumar B. (2014). Experimental study on isotope
684 fractionation of evaporating water of different initial isotopic composition. *Journal of*
685 *Radioanalytical and Nuclear Chemistry*, 302(2), <https://doi.org/10.1007/s10967-014-3368-7>
- 686 Diekmann, C. J., Schneider, M., Knippertz, P., Vries, A. J., Pfahl, S., Aemisegger, F., et al.
687 (2021). A lagrangian perspective on stable water isotopes during the West African
688 Monsoon. *Journal of Geophysical Research: Atmospheres*, 126(19), e2021JD034895.
689 <https://doi.org/10.1029/2021jd034895>
- 690 Farlin, J., Lai, C. T., & Yoshimura, K. (2013). Influence of synoptic weather events on the
691 isotopic composition of atmospheric moisture in a coastal city of the western United States.
692 *Water Resources Research*, 49(6), 3685-3696. <https://doi.org/10.1002/wrcr.20305>
- 693 Fiorella, R. P., Poulsen, C. J. & Matheny, A. M. (2018). Seasonal patterns of water cycling in a
694 deep, continental mountain valley inferred from stable water vapor isotopes. *Journal of*
695 *Geophysical Research: Atmospheres*, 123(14), 7271-7291.
696 <https://doi.org/10.1029/2017jd028093>
- 697 Fiorella, R. P., West, J. B., & Bowen, G. J. (2019). Biased estimates of the isotope ratios of
698 steady-state evaporation from the assumption of equilibrium between vapour and
699 precipitation. *Hydrological Processes*, 33(19), 2576-2590.
700 <https://doi.org/10.1002/hyp.13531>
- 701 Galewsky, J., Jensen, M. P., & Delp, J. (2022). Marine boundary layer decoupling and the stable
702 isotopic composition of water vapor. *Journal of Geophysical Research: Atmospheres*,
703 127(3), e2021JD035470. <https://doi.org/10.1029/2021jd035470>

- 704 Galewsky, J., Rella, C., Sharp, Z., Samuels, K., & Ward, D. (2011). Surface measurements of
705 upper tropospheric water vapor isotopic composition on the Chajnantor Plateau, Chile.
706 *Geophysical Research Letters*, 38(17), L17803. <https://doi.org/10.1029/2011gl048557>
- 707 Galewsky, J. Steen-Larsen, H. C., Field, R. D., Worden, J., Risi, C., & Schneider, M. (2016).
708 Stable isotopes in atmospheric water vapor and applications to the hydrologic cycle.
709 *Reviews of Geophysics*, 54(4), 809-865. <https://doi.org/10.1002/2015rg000512>
- 710 Gat, J. R. (1996). Oxygen and hydrogen isotopes in the hydrologic cycle. *Annual Review of*
711 *Earth and Planetary Sciences*, 24, 225-262. <https://doi.org/10.1146/annurev.earth.24.1.225>
- 712 Gonzalez, Y., Schneider, M., Rodriguez, S., Christner, E., Garcia, O. E., Cuevas, E., et al.
713 (2016). Detecting moisture transport pathways to the subtropical North Atlantic free
714 troposphere using paired H₂O- δ D in situ measurements. *Atmospheric Chemistry and*
715 *Physics*, 16(7), 4251-4269. <https://doi.org/10.5194/acp-16-4251-2016>
- 716 Griffis, T. J., Wood, J. D., Baker, J. M., Lee, X. H., Xiao, K., Chen, Z. C., et al. (2016).
717 Investigating the source, transport, and isotope composition of water vapor in the planetary
718 boundary layer. *Atmospheric Chemistry and Physics*, 16(8), 5139-5157.
719 <https://doi.org/10.5194/acp-16-5139-2016>
- 720 Hu, Y. B., Xiao, W., Wei, Z. W., Welp, L. R., Wen, X. F., & Lee, X. H. (2021). Determining the
721 isotopic composition of surface water vapor flux from high-frequency observations using
722 flux-gradient and keeling plot methods. *Earth and Space Science*, 8(3), e2020EA001304.
723 <https://doi.org/10.1029/2020ea001304>
- 724 Hu, Z. M., Wen, X. F., Sun, X. M., Li, L. H., Yu, G. R., Lee, X. H. & Li S. G. (2014).
725 Partitioning of evapotranspiration through oxygen isotopic measurements of water pools

- 726 and fluxes in a temperate grassland. *Journal of Geophysical Research: Biogeosciences*,
727 *119*(3), 358-371. <https://doi.org/10.1002/2013jg002367>
- 728 Huang, L. J., & Wen, X F. (2014). Temporal variations of atmospheric water vapor δD and $\delta^{18}O$
729 above an arid artificial oasis cropland in the Heihe River Basin. *Journal of Geophysical*
730 *Research: Atmospheres*, *119*(19), 11456-11476. <https://doi.org/10.1002/2014jd021891>
- 731 Huang, Y. Y., Wang, B., Li, X. F., & Wang, H. J. (2018). Changes in the influence of the
732 western Pacific subtropical high on Asian summer monsoon rainfall in the late 1990s.
733 *Climate Dynamics*, *51*(1-2), 443-455. <https://doi.org/10.1007/s00382-017-3933-1>
- 734 Kurita, N., Newman, B. D., Araguas-Araguas, L. J., & Aggarwal, P. (2012). Evaluation of
735 continuous water vapor δD and $\delta^{18}O$ measurements by off-axis integrated cavity output
736 spectroscopy. *Atmospheric Measurement Techniques*, *5*(8), 2069-2080.
737 <https://doi.org/10.5194/amt-5-2069-2012>
- 738 Lai, C.T., & Ehleringer, J. (2011). Deuterium excess reveals diurnal sources of water vapor in
739 forest air. *Oecologia*, *165*(1), 213-223. <https://doi.org/10.1007/s00442-010-1721-2>
- 740 Lai, X., Wright, J. S., Huang, W. Y., Liang, J., Lin, G. H., & Zhu, S. X. (2018). Contributions of
741 atmospheric transport and rain-vapor exchange to near-surface water vapor in the Zhanjiang
742 Mangrove Reserve, southern China: an isotopic perspective. *Atmosphere*, *9*(9), 365.
743 <https://doi.org/10.3390/atmos9090365>
- 744 Laonamsai, J., Ichiyanagi, K., Patsinghasanee, S., & Kamdee, K. (2021). Controls on stable
745 isotopic characteristics of water vapour over Thailand. *Hydrological Processes*, *35*(7),
746 e14202. <https://doi.org/10.1002/hyp.14202>

- 747 Lee, X. H., Sargent, S., Smith, R., & Tanner, B. (2005). In situ measurement of the water vapor
748 $^{18}\text{O}/^{16}\text{O}$ isotope ratio for atmospheric and ecological applications. *Journal of Atmospheric
749 and Oceanic Technology*, 22(8), 1305-1305. <https://doi.org/10.1175/JTECH9001.1a>
- 750 Lee, X. H., Smith, R., & Williams, J. (2006). Water vapour $^{18}\text{O}/^{16}\text{O}$ isotope ratio in surface air in
751 New England, USA. *Tellus Series B-Chemical and Physical Meteorology*, 58(4), 293-304.
752 <https://doi.org/10.1111/j.1600-0889.2006.00191.x>
- 753 Lee, X. H., Kim, K., & Smith R. (2007). Temporal variations of the $^{18}\text{O}/^{16}\text{O}$ signal of the whole-
754 canopy transpiration in a temperate forest. *Global Biogeochemical Cycles*, 21, GB3013.
755 <https://doi.org/10.1029/2006gb002871>
- 756 Li, Y. J., An, W. L., Pang, H. X., Wu, S. Y., Tang, Y. Y., Zhang, W. B., & Hou, S.G. (2020).
757 Variations of stable isotopic composition in atmospheric water vapor and their controlling
758 factors-a 6-year continuous sampling study in Nanjing, eastern China. *Journal of
759 Geophysical Research: Atmospheres*, 125, e2019JD031697.
760 <https://doi.org/10.1029/2019jd031697>
- 761 Luo, J. S., Sun, Y. H., Wang, Y. G., Xie, Z. H., & Meng, L. D. (2021). Cenozoic tectonic
762 evolution of the eastern Liaodong Bay sub-basin, Bohai Bay basin, eastern China-
763 Constraints from seismic data. *Marine and Petroleum Geology*, 134, 105346.
764 <https://doi.org/10.1016/j.marpetgeo.2021.105346>
- 765 Mao, D.H., He, X.Y., Wang, Z.M., Tian, Y.L., Xiang, H.X., Yu, H., et al. (2019). Diverse
766 policies leading to contrasting impacts on land cover and ecosystem services in Northeast
767 China. *Journal of Cleaner Production*, 240, 117961.
768 <https://doi.org/10.1016/j.jclepro.2019.117961>

- 769 Mao, D.H., Wang, Z.M., Du, B.J., Li, L., Tian, Y.L., Zeng, Y., et al. (2020). National wetland
770 mapping in China: A new product resulting from object based and hierarchical classification
771 of Landsat 8 OLI images. *ISPRS Journal of Photogrammetry and Remote Sensing*, 164, 11-
772 25 <https://doi.org/10.1016/j.isprsjprs.2020.03.020>
- 773 Mercer, J. J., Liefert, D. T., & Williams, D. G. (2020). Atmospheric vapour and precipitation are
774 not in isotopic equilibrium in a continental mountain environment. *Hydrological Processes*,
775 34(14), 3078-3101. <https://doi.org/10.1002/hyp.13775>
- 776 Merlivat, L., & Jouzel, J. (1979). Global climatic interperetation of the deuterium ¹⁸O
777 relationship for precipitation. *Journal of Geophysical Research: Oceans*, 84(C8), 5029-
778 5033. <https://doi.org/10.1029/jc084ic08p05029>
- 779 Munksgaard, N. C., Zwart, C., Haig, J., Cernusak, L. A., & Bird, M. I. (2020). Coupled rainfall
780 and water vapour stable isotope time series reveal tropical atmospheric processes on
781 multiple timescales. *Hydrological Processes*, 34(1), 111-124.
782 <https://doi.org/10.1002/hyp.13576>
- 783 NFGA. (2010). National Wetland Survey Statistics Report. National Forestrty and Grassland
784 Administration (in Chinese). <https://www.forestry.gov.cn>
- 785 Noone, D. (2012). Pairing measurements of the water vapor isotope ratio with humidity to
786 deduce atmospheric moistening and dehydration in the tropical midtroposphere. *Journal of*
787 *Climate*, 25(13), 4476-4494. <https://doi.org/10.1175/jcli-d-11-00582.1>
- 788 Parkes, S. D., McCabe, M. F., Griffiths, A. D., Wang, L. X., Chambers, S., Ershadi, A., et al.
789 (2017). Response of water vapour *D-excess* to land-atmosphere interactions in a semi-arid
790 environment. *Hydrology and Earth System Sciences*, 21(1), 533-548.
791 <https://doi.org/10.5194/hess-21-533-2017>

- 792 Salamalikis, V., Argiriou, A. A., & Dotsika, E. (2015). Stable isotopic composition of
793 atmospheric water vapor in Patras, Greece: a concentration weighted trajectory approach.
794 *Atmospheric Research*, 152, 93-104. <https://doi.org/10.1016/j.atmosres.2014.02.021>
- 795 Steen-Larsen, H. C., Johnsen, S. J., Masson-Delmotte, V., Stenni, B., Risi, C., Sodemann, H., et
796 al. (2013). Continuous monitoring of summer surface water vapor isotopic composition
797 above the Greenland Ice Sheet. *Atmospheric Chemistry and Physics*, 13(9), 4815-4828.
798 <https://doi.org/10.5194/acp-13-4815-2013>
- 799 Steen-Larsen, H. C., Masson-Delmotte, V., Hirabayashi, M., Winkler, R., Satow, K., Prie, F., et
800 al. (2014b). What controls the isotopic composition of Greenland surface snow? *Climate of*
801 *the Past*, 10(1), 377-392. <https://doi.org/10.5194/cp-10-377-2014>
- 802 Steen-Larsen, H. C., Sveinbjörnsdóttir, A. E., Jonsson, T., Ritter, F., Bonne, J. L., Masson-
803 Delmotte, V., et al. (2015). Moisture sources and synoptic to seasonal variability of North
804 Atlantic water vapor isotopic composition. *Journal of Geophysical Research: Atmospheres*,
805 120(12), 5757-5774. <https://doi.org/10.1002/2015jd023234>
- 806 Steen-Larsen, H. C., Sveinbjörnsdóttir, A. E., Peters, A. J., Masson-Delmotte, V., Guishard, M.
807 P., Hsiao, G., et al. (2014a). Climatic controls on water vapor deuterium excess in the
808 marine boundary layer of the North Atlantic based on 500 days of in situ, continuous
809 measurements. *Atmospheric Chemistry and Physics*, 14(15), 7741-7756.
810 <https://doi.org/10.5194/acp-14-7741-2014>
- 811 Sturm, P., & Knohl, A. (2010). Water vapor $\delta^2\text{H}$ and $\delta^{18}\text{O}$ measurements using off-axis
812 integrated cavity output spectroscopy. *Atmospheric Measurement Techniques*, 3(1), 67-77.
813 <https://doi.org/10.5194/amt-3-67-2010>

- 814 Tian, L. D., Yu, W. S., Schuster, P. F., Wen, R., Cai, Z. Y., Wang, D., et al. (2020). Control of
815 seasonal water vapor isotope variations at Lhasa, southern Tibetan Plateau. *Journal of*
816 *Hydrology*, 580, 124237. <https://doi.org/10.1016/j.jhydrol.2019.124237>
- 817 Tremoy, G., Vimeux, F., Vimeux, F., Souley, I., Risi, C., Favreau, G., & Oi, M. (2014).
818 Clustering mesoscale convective systems with laser-based water vapor delta O-18
819 monitoring in Niamey (Niger). *Journal of Geophysical Research: Atmospheres*, 119(9),
820 5079-5103. <https://doi.org/10.1002/2013jd020968>
- 821 Uemura, R., Matsui, Y., Yoshimura, K., Motoyama, H., & Yoshida, N. (2008). Evidence of
822 deuterium excess in water vapor as an indicator of ocean surface conditions. *Journal of*
823 *Geophysical Research: Atmospheres*, 113, D19114. <https://doi.org/10.1029/2008jd010209>
- 824 Vuille, M., Bradley, R. S., Werner, M., Healy, R., & Keimig, F. (2003). Modeling $\delta^{18}\text{O}$ in
825 precipitation over the tropical Americas: interannual variability and climatic controls.
826 *Journal of Geophysical Research: Atmospheres*, 108(D6), 4174.
827 <https://doi.org/10.1029/2001jd002038>
- 828 Wang, G. D., Wang, M., Lu, X. G., & Jiang, M. (2016). Surface elevation change and
829 susceptibility of coastal wetlands to sea level rise in Liaohe Delta, China. *Estuarine Coastal*
830 *and Shelf Science*, 180, 204-211. <https://doi.org/10.1016/j.ecss.2016.07.011>
- 831 Wang, G. Y., Lan, H. M., & Liu, Z. F. (2021). Stable isotope record of super typhoon Lekima
832 (2019). *Atmospheric Research*, 264, 264, 105822.
833 <https://doi.org/10.1016/j.atmosres.2021.105822>
- 834 Wei, Z. W., & Lee, X. H. (2019). The utility of near-surface water vapor deuterium excess as an
835 indicator of atmospheric moisture source. *Journal of Hydrology*, 577, 123923.
836 <https://doi.org/10.1016/j.jhydrol.2019.123923>

- 837 Wei, Z. W., Yoshimura, K., Okazaki, A., Kim, W., Liu, Z. F., & Yokoi, M. (2015). Partitioning
838 of evapotranspiration using high-frequency water vapor isotopic measurement over a rice
839 paddy field. *Water Resources Research*, 51(5), 3716-3729.
840 <https://doi.org/10.1002/2014wr016737>
- 841 Welp, L. R., Lee, X. H., Griffis, T. J., Wen, X. F., Xiao, W., Li, S. G., et al. (2012). A meta-
842 analysis of water vapor deuterium-excess in the midlatitude atmospheric surface layer.
843 *Global Biogeochemical Cycles*, 26, GB3021. <https://doi.org/10.1029/2011gb004246>
- 844 Wen, X. F., Lee, X. H., Sun, X. M., Wang, J. L., Hu, Z. M., Li, S.G., & Yu, G.R. (2012). Dew
845 water isotopic ratios and their relationships to ecosystem water pools and fluxes in a
846 cropland and a grassland in China. *Oecologia*, 168(2), 549-561.
847 <https://doi.org/10.1007/s00442-011-2091-0>
- 848 Wen, X. F., Sun, X. M., Zhang, S. C., Yu, G. R., Sargent, S. D., & Lee, X. H. (2008).
849 Continuous measurement of water vapor D/H and $^{18}\text{O}/^{16}\text{O}$ isotope ratios in the atmosphere.
850 *Journal of Hydrology*, 349(3-4), 489-500. <https://doi.org/10.1016/j.jhydrol.2007.11.021>
- 851 Wen, X. F., Zhang, S. C., Sun, X. M., Yu, G. R., & Lee, X. H. (2010). Water vapor and
852 precipitation isotope ratios in Beijing, China. *Journal of Geophysical Research:*
853 *Atmospheres*, 115, D1103. <https://doi.org/10.1029/2009jd012408>
- 854 Wu, H. W, Li, X. Y., Zhang, J. M., Li, J., Liu, J. Z., Tian, L. H., & Fu, C.S. (2019). Stable
855 isotopes of atmospheric water vapour and precipitation in the northeast Qinghai-Tibetan
856 Plateau. *Hydrological Processes*, 33(23), 2997-3009. <https://doi.org/10.1002/hyp.13541>
- 857 Wu, X. X., Chen, F. L., Liu, X. Y, Wang, S. J., Zhang, M. J., Zhu, G. F., et al. (2021). The
858 significance of hydrogen and oxygen stable isotopes in the water vapor source in Dingxi
859 area. *Water*, 13(17), 2374. <https://doi.org/10.3390/w13172374>

- 860 Xiao, W., Lee, X. H., Hu, Y. B., Liu, S. D., Wang, W., Wen, X. F., et al. (2017). An
861 experimental investigation of kinetic fractionation of open-water evaporation over a large
862 lake. *Journal of Geophysical Research: Atmospheres*, 122(21), 11651-11663.
863 <https://doi.org/10.1002/2017jd026774>
- 864 Xu, T., Pang, H. X., Zhan, Z. J., Zhang, W. B., Guo, H. W., Wu, S. Y., & Hou, S. G. (2022).
865 Water vapor isotopes indicating rapid shift among multiple moisture sources for the 2018-
866 2019 winter extreme precipitation events in southeastern China. *Hydrology and Earth
867 System Sciences*, 26(1), 117-127. <https://doi.org/10.5194/hess-26-117-2022>
- 868 Zhang, S. C., Sun X. M., Wang J. L., Yu, G. R., Wen, X. F. (2011). Short-term variations of
869 vapor isotope ratios reveal the influence of atmospheric processes. *Journal of Geographical
870 Sciences*, 21(3), 401-416. <https://doi.org/10.1007/s11442-011-0853-6>
- 871 Zhao, L., Wang, L., Liu, X., Xiao, H., Ruan, Y., & Zhou, M. (2014). The patterns and
872 implications of diurnal variations in the d-excess of plant water, shallow soil water and air
873 moisture. *Hydrology and Earth System Sciences*, 18(10), 4129-4151.
874 <https://doi.org/10.5194/hess-18-4129-2014>